Parallel-Elastic Actuation with Reactive Latch Elevates Robotic Hopping Performance: Jump Height and Continuity

Songnan Bai, Runze Ding, Song Li, Student Member, Ruihan Jia, Ruobing Wang, Zhiyuan Zhang, Fangzheng Wang and Pakpong Chirarattananon, Member, IEEE

***Abstract*—While many animals exhibit impressive hopping capabilities, machines have struggled to match their performance. Current hopping robots face limitations in power density, energy efficiency, and control stability. Here, we present a parallel-elastic actuation mechanism with a reactive latch that optimizes energy transfer, enabling a legged robot to achieve hopping heights and continuity previously unattainable. This mechanism efficiently stores and releases energy, extending the actuation period over the aerial phase while minimizing stance time. Our robot achieves a maximum hopping height of 3.6 meters, surpassing both human and animal records while demonstrating sustained, high-frequency hopping cycles with minimal power requirement. By integrating inertia-based onboard sensorimotor autonomy, we demonstrate stable, controlled hopping in environments without external aid. These results represent a step toward bridging the performance gap between biological and robotic locomotion, with potential to influence the design of future legged systems.**

***Index Terms*—Parallel-elastic actuation, hopping, legged robots, spring-loaded inverted pendulum (SLIP).**

I. INTRODUCTION

HOPPING is observed in only a few mammalian families, notably among species such as kangaroos, bush babies (Galagos) and kangaroo rats [1]. These animals exhibit a distinct saltatory locomotion, performing successive jumps exclusively with their hindlimbs, while their forelimbs remain uninvolved [2]. This locomotion features an extended aerial phase and substantial vertical displacement per stride, enabling efficient traversal of unstructured and otherwise inaccessible terrains [3]. The considerable vertical reach not only allows access to elevated spaces typically reserved for flying species but also provides an effective means of escaping predators through erratic and unpredictable trajectories [4], [5]. Moreover, hopping is observed to be energetically efficient at moderate speeds, particularly in large kangaroos, which can maintain their metabolic cost above a certain hopping velocity, unlike quadrupedal mammals, whose oxygen consumption increases with speed [1], [6]–[9]. This unique efficiency contributes to the evolutionary success of hopping in specific large mammals.

Efforts to artificially replicate biological hopping locomotion have led to the development of various jumping [10]–[21] and hopping [22]–[33] robots powered by electric motors, elastomer, shape-memory alloy [11] or chemical combustion [34], [35]. However, few of these robots can simultaneously match the agile, continuous jumping ability and impressive heights achieved by their biological counterparts. For example, Galago can achieve a vertical jump of 2.25 m [3], [36], equivalent to six times its body length. During continuous hopping climbs, it can ascend at a rate of 2.24 ms^{-1}, with each hop reaching 1.74 m [31], [36].

One of the challenges in replicating biological hopping lies in delivering sufficient power during the brief stance phase [37] and sustaining this frequent power delivery across consecutive jumps. While current quadruped and biped robots can manage repetitive motions, their instantaneous power output and achievable jump heights remain significantly below biological counterparts. To overcome these limitations, robotic designs have incorporated various elastic configurations to enhance jumping performance [22], [24], [28]–[33], [38]–[40]. A notable approach integrates series-elastic actuation with mechanical advantage adaptation (SE+MA) for power modulation [23], [31], [32], [40], [41], demonstrating improved agility in hopping. Nevertheless, these robots remain constrained by the actuation power available during the stance phase, and thus still fall short of the extreme jumps observed in nature.

In addition to actuation, control remains a critical challenge for robotic hopping, requiring robust stabilization, precise attitude regulation, and reliable feedback. Model-based hopping controllers have enabled effective directional control by manipulating touchdown angles, leading to aggressive yet stable hopping maneuvers [24], [42], [43]. However, achieving robust state estimation remains a major hurdle. Unlike aerial robots, hopping robots spend most of its time in free fall, preventing standard sensor fusion algorithms from accurately deducing the robot's orientation relative to gravity. In addition, impulsive accelerations during ground contact further disrupt conventional sensor fusion [44]. Together, these factors prevent the use of standard inertial-based state estimation techniques for stable, long-term hopping [24], [40]. A similar challenge

---

This work was supported by the Start-up Research Fund of Southeast University (grant no. RF1028626068 to R.Z.), the Shenzhen-Hong Kong-Macau Science and Technology Project (Category C) under (grant no. SGDX20220530111401009 to P.C.), the Research Grants Council of the Hong Kong Special Administrative Region of China (grant no. CityU 11217923, CityU 11209024, and PolyU R5006-23 to P.C.), and the Start-up Grant from the Department of Mechanical and Industrial Engineering, University of Toronto (to P.C.). Songnan Bai is with the Department of Civil Engineering, University of Hong Kong, Hong Kong SAR, China. Runze Ding is with the School of Automation, Southeast University, Nanjing, China. Song Li, Ruihan Jia, Ruobing Wang, Zhiyuan Zhang and Fangzheng Wang are with the Department of Biomedical Engineering, City University of Hong Kong, Hong Kong SAR, China. Pakpong Chirarattananon is with the Department of Mechanical & Industrial Engineering, University of Toronto, Toronto, ON M5S 3G8, Canada. Corresponding author: Pakpong Chirarattananon, Email: p.chirarattananon@utoronto.ca

is seen in highly dynamic systems, such as racing drones. To compensate, these systems typically rely on external positioning and attitude feedback rather than inertial sensors alone [45]–[47]. This fundamental limitation has largely confined continuously hopping robots to controlled laboratory environments with external sensing infrastructure.

In this work, we analyze fundamental actuation limits for hopping robots in terms of both achievable height and continuity. Our findings show that, leveraging the parallel-elastic actuation mechanism, the large power demand for consecutive high hops can be mitigated by prolonging the actuation period into the aerial phase and by efficiently recycling energy across hopping cycles. Although the concept of aerial-phase energy loading and recovery was proposed decades ago [48]–[52], no prior robot has been designed to achieve both exceptionally high jumping height and high hopping continuity [31].

Based on these insights, we developed a 54-gram, parallel-elastic hopping robot with a reactive latch mechanism (Fig. 2(a)). The robot can preload the elastomer during the aerial phase and mechanically releases the stored energy synchronously with landing. In contrast, conventional parallel-elastic systems such as the EPFL Jumper [21] or MultiMo-Bat [19] are designed to load their springs on the ground and are unable to release the energy in a timely manner upon landing, preventing continuous hopping. While our design shares some similarities with the bow leg low-gravity hoppers [48], [52], previous robots have not exploited these principles to achieve superior jump heights and continuity. In addition, our robot uniquely enables modulation of the stored elastic energy, allowing control over a wide range of hopping heights. Finally, by efficiently recycling the kinetic energy from landing [24], [32], [48], [52], our design reduces actuator power demands, permitting high jumps even with low-power motors.

To enable stable hopping, our robot employs four propellers dedicated to torque generation and attitude regulation during the aerial phase. In contrast to the thrust-based hopping robot in [24], which strategically increases thrust after takeoff to compensate for energy losses during stance (termed "powered ascent"), our robot adopts a similar configuration but thrust is minimized throughout the entire aerial phase without "powered ascent". Residual thrust is present mainly for attitude control (see [24] for the details of the power distribution method). The rotor power contributes only about 15% of the jump height, and the hopping motion remains predominantly ballistic. Minimizing aerodynamic thrust generation also enhances hopping continuity [24], [53], [54]. In addition to these mechanical innovations, we address the challenge of state estimation for dynamic hopping locomotion. Previous solutions have relied on external motion capture systems for attitude estimation [24], [32], LiDAR [44], or required additional sensors to measure leg extension [40] or ground orientation [50]. In contrast, we developed a model-based state estimator that leverages the predictable dynamics of each hop cycle. By relating the robot's motion at takeoff and landing, our approach enables accurate onboard estimation of attitude and position using only an inertial measurement unit (IMU), without requiring any additional onboard or external sensors. This advance allows the robot to achieve sustained, stable hopping in real-world environments using an inertial sensor and control alone. Leveraging these integrated design, estimation, and control strategies, our robot demonstrates 3.6-meter hops, surpassing both robotic and biological records while operating entirely on onboard sensing and control.

Throughout this paper, references to figures and tables prefixed with "S" (e.g., Fig. S1, Table S1) denote items presented in the Supplementary Materials.

II. POWER LIMITS FOR HIGH AND CONTINUOUS HOPS

Hopping performance can be characterized by hopping height and continuity, both of which are fundamentally constrained by the actuator power. We quantify continuity using the normalized hopping frequency, f^*, defined as the ratio of the actual hopping frequency (f) to the theoretical maximum ballistic frequency $(1/\sqrt{8h/g})$ at a given height (h): $f^* = f\sqrt{8h/g}$, where g is the gravitational acceleration. A normalized hopping frequency of 1 represents the ballistic limit [31], where the jumper spends no time in stance and follows a purely ballistic trajectory in air. Unlike vertical jumping agility [31] or hopping agility [24], [31], f^* is independent of jump height.

To achieve a hop height h, a jumper of mass m must accelerate to a takeoff speed of at least $\sqrt{2gh}$, delivering energy of mgh. Without energy recycling [24], [31], [43] and with limited leg power $P_{\max}$, power output constrains the stance phase push off time, thereby limiting the achievable hopping frequency. The greater the power output, the shorter the required push off time, and consequently, the higher f^*. This trade-off makes it challenging to achieve both high hop and high normalized hopping frequency simultaneously as shown in Fig. 1(a). The specific performance limits and achievable combinations of height and normalized frequency depend critically on the leg actuation mechanism employed.

We first consider the case of direct-drive jumpers, in which legs are powered by muscles or motors coupled via rigid transmissions with minimal elastic energy storage (Fig. 1(b)). For such systems, the maximum hopping height $h_{\max}$ is attained when the leg actuators maintain maximum output power $P_{\max}$ throughout the takeoff stroke [56]. In this scenario, the maximum height depends on the power density $P_{\max}/m$ and the available leg stroke l_{leg}. In the absence of air drag, $h_{\max}$ is proportional to $(l_{\text{leg}}P_{\max}/m)^{2/3}$ (see Appendix A). For these jumpers, their optimal f^* (see Equation (47)) depends on both h and $P_{\max}/m$ (see Fig. 1(c)). Higher jumps enable higher normalized frequency, but achieving both simultaneously requires substantially increased actuator power.

Reported hopping heights of direct-drive robots [26], [27], [57]–[59] fall far below the theoretical limit, ranging between 0.05 and 0.2 of $h_{\max}$ (Fig. S1 and Table S1). This discrepancy arises primarily from motor load fluctuations, hindering them from sustaining maximum output power. Efforts to increase power density [26], [27], [29], [39], [57], [58] of actuators have shown progress, with some reaching up to 468 Wm/kg [21], [26]. Despite these, the realized heights remain limited, reaching only 0.82 m or 15% of $h_{\max}$ (Fig. S1). Similarly, the f^* ranges from 0.70 to 0.74 (Fig. 1(c)), well below the theoretical optimum of 0.98 (refer to (47) and Table S1).

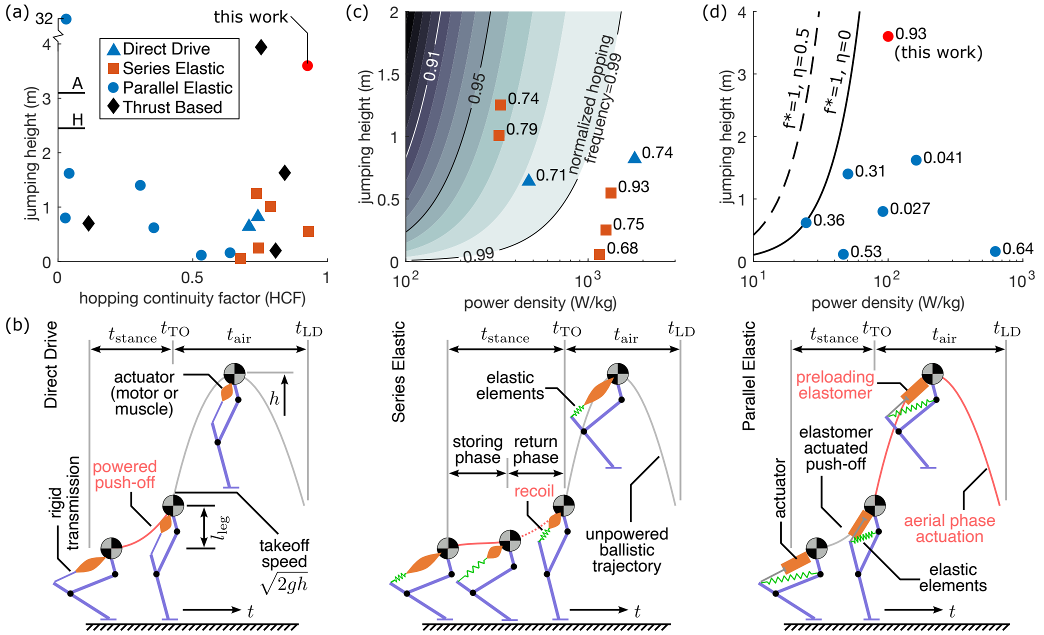

Fig. 1. (a) Hopping height versus normalized hopping frequency f^* of robots with various actuation mechanisms. The labels "A" and "H" on the left indicate the jumping height records of animals and humans [55]. (b) Schematic diagrams illustrating the behaviors of direct-drive, series-elastic and parallel elastic robots. (c) Hopping height of direct-drive and series-elastic robots versus power density. The contour map indicates the modeled normalized hopping frequency limit when the energy recycling efficiency is zero. The numbers next to the points indicate the corresponding normalized hopping frequency. (d) Hopping height of parallel-elastic robots versus power density. The lines denote the height limit of the mechanism when operated at optimal continuity ($f^* = 1$) when the energy recycling efficiency η is 0 and 0.5. The numbers next to the points indicate the corresponding normalized hopping frequency.

Incorporating elastic elements into the leg mechanism enhances jumping and hopping performance in both animals [6], [8], [36], [60]–[62] and robots. These mechanisms are primarily categorized as series-elastic [6], [8], [28], [31]–[33], [36], [55], [60], [62], [63] and parallel-elastic [10], [16], [18], [19], [21], [22], [29], [38], [39], [48], [52], [64]–[68] (see Fig. 1(b)). Elastic elements offer two key advantages: (i) elastic elements recycle energy from previous landings, reducing the power demands for continuous hopping, and (ii) they can gradually store actuator energy and release it rapidly via recoil, enabling high burst power.

An example of series-elastic robots is Salto [31], [32], which uses a stroke-dependent transmission. During the beginning of its push-off stroke (the storing phase) while in contact with the ground, the mechanical advantage is decreased, reducing leg extension force and allowing the elastomer to be loaded with a force exceeding the robot's weight over an extended period. In the return phase, both the motor and elastomer contribute to propulsion as the mechanism advantage increases (Fig. 1(b)).

Unlike direct-drive jumpers, series-elastic robots are not fundamentally limited in jumping height since more energy can be stored by extending the duration of the storing phase [31]. However, achieving higher jumps with low power density reduces hopping continuity as the stance time becomes the limiting factor. Assume the time spent in the return phase is negligible, the total stance time is dominated by the storing phase, which is bounded from below by $(1-\eta)mgh/P_{\max}$, where η represents the efficiency of energy recycling from previous landings. Thus, the achievable f^* for series-elastic jumpers can be approximated by the same relationship as for direct-drive jumpers as shown in Fig. 1(c) and described by (48) in Appendix B, but with the energy required scaled by $1-\eta$. When $\eta = 0$, no energy is recovered and the result reduces to the direct-drive case. As η increases, the maximum achievable f^* improves due to the reduced energy demand.

In contrast, parallel-elastic robots inherently excel at continuous hopping [31], [48], [52]. In these systems, actuators are connected to elastomer in parallel, allowing the spring to be preloaded during the aerial phase without the ground contact [48], [52], [64] (see Fig. 1(b)). As a result, their stance phase consists solely of the rapid recoil of the elastomer, with its duration dictated by leg stiffness: $t_{\text{stance}} < \pi\sqrt{m/k}$, independent of actuator power. By employing stiff springs, the normalized hopping frequency can approach unity.

In this regime ($f^* = 1$), the actuator only has the aerial phase to preload the elastomer. The duration depends on the hop height ($2\sqrt{2h/g}$), which imposes a fundamental limit on maximum continuous hop height based on actuator power density and the efficiency of energy recycling η, as given in (49) (illustrated in Fig. 1(d) and detailed in Appendix B). The model suggests that increasing η is a highly effective method for increasing height. However, only a limited number of parallel-elastic robots [48], [52] are mechanically capable of leveraging this advantage. If the requirement for hopping continuity is relaxed, the stance phase can be lengthened to provide the actuator more time to load the elastomer. Consequently, the maximum achievable height increases as f^* decreases. In theory, as f^* approaches zero, the stance phase becomes arbitrarily long, and there is no strict upper bound on hop height (similar to that of series-elastic robots). This limit is realized in robots designed for intermittent, high jumps, which typically employ latch mechanisms to maximize energy storage during prolonged stance phases [10], [16], [18]–[21]. These robots remain grounded for 2 to 120 seconds while loading their springs, resulting in low normalized frequency values (0.02 to 0.4), but can achieve impressive jump heights, ranging from 0.6 to 32 meters, even when powered by relatively low-power motors (Fig. 1(a) and Table S2).

Early attempts to leverage parallel-elastic mechanisms for continuous hopping include the bow-leg robot [48] and ParkourBot [52]. They preload their springs during the aerial phase and mechanically release them upon landing. However, these robots display relatively low hopping height (less than 0.5 m), thus not fully demonstrating the potential of parallel-elastic designs. Other related mechanisms, such as the S-curve series-elastic actuator face similar limitations. The mechanically tethered catapult system uses kinematic singularities for latching and aerial-phase loading, demonstrates restricted performance (maximum height 0.33 m, $f^* = 0.29$) and its mechanical efficiency remains low (12% energy transfer during push-off). This is largely due to the fact that the motor must be continuously powered, even when the spring is already preloaded. Subsequent designs, such as the inverted cam hopper [64], use a latched release mechanism with a specific fixed interval, achieving only moderate normalized hopping frequency ($f^* = 0.53$) and low, fixed hopping heights 0.12 m, see Fig. 1(a)) because of the mismatched timing between energy release and hopping frequency.

Thus far, few robots capable of continuous hopping have exceeded the baseline height of direct-drive systems ($h_{\max}$), and most still fall short of biological benchmarks such as humans (2.45 m) and red kangaroo (Macropus rufus, 3.1 m [55]). A notable exception is a new class of thrust-based hopping robots, which have achieved heights from 1.6 to 4 m [24], [54], f^* ranging from 0.11 to 0.84 [24], [43], [53], [54], depending on control strategy (see Fig. 1(a)). However, achieving high hops require aerodynamic thrust comparable to body weight [54], resulting in power densities typically exceeding 480 W/kg, on par with those of aerial robots [69]. By contrast, the power densities of parallel-elastic jumping robots are as low as 28 W/kg [19] (see Table S1). However, no previous robot with series- or parallel-elastic actuation has demonstrated both high hopping height and high continuity.

III. PARALLEL-ELASTIC HOPPING ROBOT WITH REACTIVE LATCH MECHANISM

This study presents a 54-gram parallel-elastic hopping robot equipped with a reactive latch mechanism, capable of high hops with high continuity (Movie S1). The robot integrates a quadcopter with maximum thrust of 42 gf mainly for aerial attitude regulation with a leg mechanism for hopping actuation (see Fig. 2(a) and Appendix C for detailed design). Unlike other thrust-based hoppers [54], [70], the proposed robot achieves hopping motion through direct leg actuation rather than thrusters. This enables the robot to rival the performance of thrust-based robots in both height and continuity, while operating at substantially lower power density.

The leg mechanism is powered by a geared motor, which drives a winch through two spur gears. The winch shaft is mounted on a hinge, allowing it to pivot for gear engagement and disengagement (Fig. 2(b) and (c)). During the aerial phase, the motor rotates the winch to preload an elastomer parallel to the telescopic leg via a cable. The cable tension keeps the gears engaged. Upon landing, the impact compresses the leg, further stretching the elastomer while slackening the cable. This causes gear disengagement, decoupling the winch from the motor. As a result, the stored elastic potential energy is released during the stance phase, propelling the robot into the jump—functioning as a latch. Continuous jumping or hopping is achieved by cyclically preloading the elastomer in midair by a controlled length (Δl_{load}) and passively releasing the energy upon landing. This parallel-elastic actuation extends the actuation period (Δt_{load}) to the entire aerial phase without prolonging the stance phase duration (Fig. 2(d) and (e)), thus accomplishing both high hops and high continuity.

To ensure the loaded cable can be timely unwinded during the short stance phase, an auxiliary winch, spring and cable were employed to assist and accelerate the cable unwinding in stance phase (see Fig. 2(a), (b) and Fig. 10). Near the hinge, an auxiliary cable is linked to the winch shaft, in series with the auxiliary spring—a rubber band with a low elastic constant (Fig. 10(c)). On the other end, the auxiliary spring is fixed on the leg frame over a fixed pulley (Fig. 2(a), omitted from in Fig. 2(b) and Fig. 10 for simplicity). When the leg elastomer is loaded, the auxiliary winch is simultaneously loaded, generating a downward pulling force f_{a} and a torque τ_{a} on the winch shaft (Fig. 10(c)).

Upon landing, tension f_{a} disengages the gears. The winch shaft becomes free to rotate. In the meantime, τ_{a} rotates the shaft to unwind the primary and auxiliary cables from the winch. To avoid cable tangling, we integrated another compliant element (tension keeper, see Fig. 2(a), Fig. 10(b), and Movie S2) to apply an out-of-plane pulling force on the cable to create a small tension during the gear disengagement.

The setting and elastic constant of the auxiliary spring (refer to Tables S3 and S4 for the robot's design parameters) are selected according to the setting of the leg elastomer and satisfy specific criteria (refer to Appendix D). The developed parallel-elastic actuation mechanism efficiently recycles landing kinetic energy. The cable-driven leg design is principally similar to that used in the bow leg mechanism [48], [52]. It allows impulsive leg compression at landing, which further loads the elastomer from its preloaded state. This process absorbs landing kinetic energy and protects the robot from high-speed ground collisions. During takeoff, all energy stored in the elastomer is released by elastic recoil, propelling the robot into the air. This energy recovery mechanism further enhances the robot's high hop capacity (see Movie S2 for demonstration of continuous hopping). To evaluate the energy recycling efficiency of the leg mechanism, we conducted 28 drop tests with various drop height and Δl_{load} (see Appendix H for details). The results show that the robot is able to convert 79% of the landing kinetic energy and preloaded elastic potential energy into takeoff kinetic energy. When the takeoff kinetic energy is marginally higher than the landing kinetic energy (leading to approximately constant hopping height), the preloaded elastic potential energy in each jump

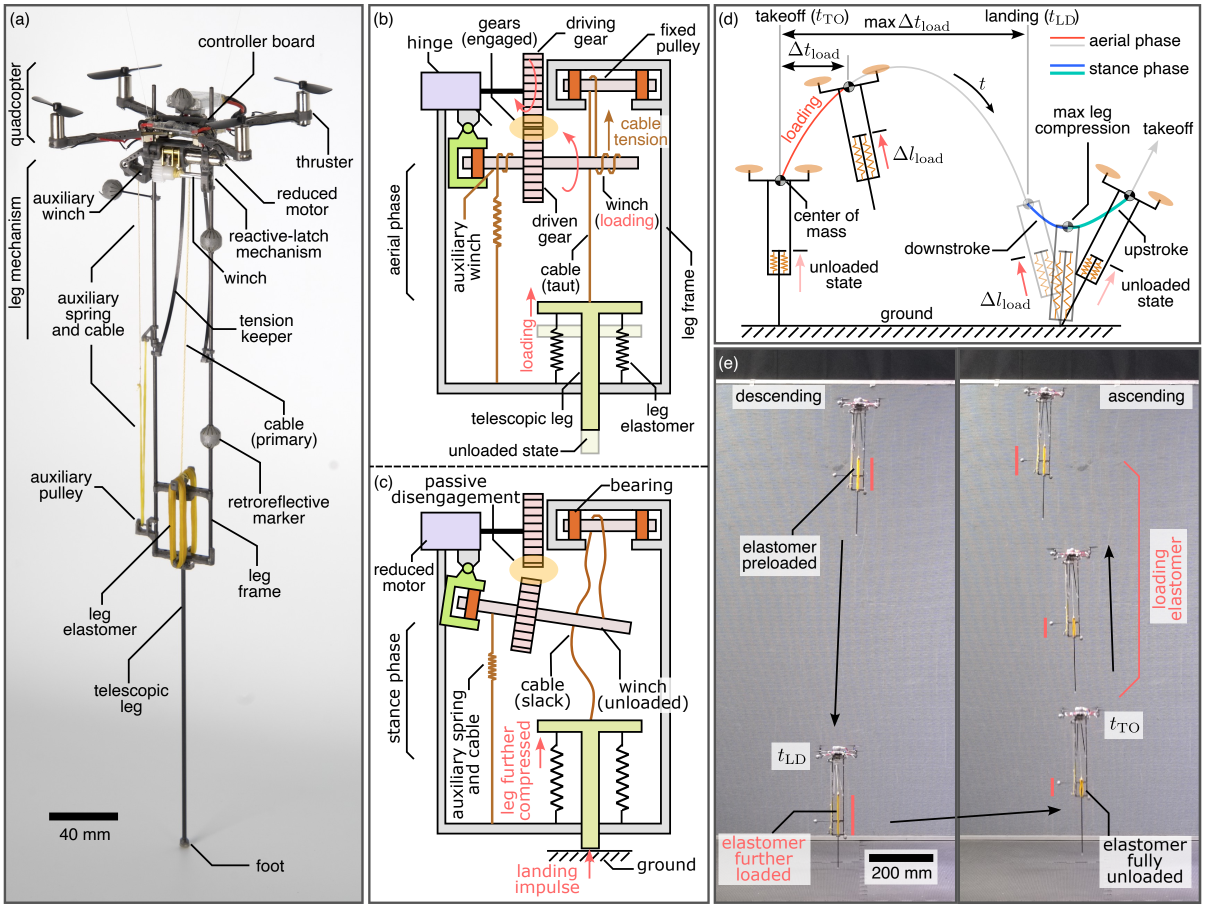

Fig. 2. (a) Photograph of the hopping robot. (b) and (c) Schematic diagrams illustrating the structure and working principles of the reactive latch mechanism (the quadcopter, tension keeper, paw and the stoppers are omitted, refer to Fig. 10 for detailed photo and diagram). The upper drawing (b) shows the elastomer loading process. The bottom drawing (c) illustrates the moment the robot lands and the impulse from the ground further extends the elastomer. (d) A diagram illustrating two phases of the continuous jumping locomotion and the midair leg actuation. (e) Composite photos demonstrating the elastomer loading through a hopping cycle. The red scale bars denote approximate elastomer lengths.

accounts for ∼28% of the takeoff kinetic energy, indicating an energy recycling efficiency of $\mu = 0.70 \pm 0.04$ (Fig. S11(b)).

The model in Fig. 1(d) presented a height limit for parallel-elastic hopping robots (when hopping at $f^* = 1$) as a function of power density (see Appendix B and (49)). However, in practice, the robot experiences various forms of energy dissipation, including friction, elastic hysteresis, and air drag. These factors increase the energy required for takeoff beyond mgh. By modeling these effects (Appendix F), the analysis shows that the hopping height increases with leg stiffness, although this also raises the power requirement. Balancing these factors, the robot is expected to achieve a hopping height of 3.0 m, with a power consumption of 1.90 W (leg motor power) at the equilibrium (Fig. S2(d), blue solid curve, the curve terminate at the predicted maximum jumping height of 3.0 m).

IV. HOPPING DYNAMICS

The dynamics of the developed robot have some similarities with the thrust-based robotic hopper [24]. The hopping motion consists of two main phases: aerial and stance, with takeoff (t_TO) and landing (t_LD) serving as key events, as illustrated in Fig. 2(d) and Fig. 3(a). Throughout the aerial phase, the robot minimizes its propelling thrust and sustains its attitude regulation capacity [24]. Unlike previous thrust-based hopping robots [24], this design eliminates the powered ascent phase, allowing the robot to follow a purely ballistic trajectory between takeoff and landing.

A. Aerial Phase Dynamics

In aerial phase, the thrusters are minimally actuated and mainly used for attitude control [24]. The translational motion of the robot is approximately ballistic and governed by:

$$m\ddot{\mathbf{p}} = -mg\mathbf{e}_3 - {}^1\!/_2 C_\mathrm{d}\rho S\,|\dot{z}|\,\dot{z}\mathbf{e}_3, \tag{1}$$

where $\mathbf{p} = [x, y, z]$ is the position, z is the altitude, $\mathbf{e}_3 = [0, 0, 1]^\mathrm{T}$ is a base vector, $-mg\mathbf{e}_3$ is the weight, and the last term, inherited from (62) in Appendix F, is the aerodynamic drag (horizontal components neglected for near-vertical hops).

Adopting (1), the hopping height and landing state (velocity and location) can be estimated according to the takeoff state (see Section IV-B below).

Meanwhile, the attitude dynamics is independent of the translation and described by Euler's rotation equations as

$$\boldsymbol{\tau}_\mathrm{p} = \mathbf{I}\dot{\boldsymbol{\omega}} + \boldsymbol{\omega} \times \mathbf{I}\boldsymbol{\omega}, \tag{2}$$

where $\boldsymbol{\tau}_{\mathrm{p}}$ is propulsion torque, $\mathbf{I} = \mathrm{diag}\left(I_x, I_y, I_z\right)$ is the inertia tensor, and $\boldsymbol{\omega}$ is the body-centric angular velocity. The attitude of the robot is represented by a rotation matrix $\mathbf{R}$, mapping the body-fixed frame to the inertial frame.

B. Landing State Prediction

Herein, we employ an index n to label a hopping cycle. From the takeoff of cycle $n-1$ to the landing of the next cycle ($t_{\mathrm{TO}}|_{n-1}$ to $t_{\mathrm{LD}}|_{n}$), the robot follows a ballistic trajectory with air drag ((1)). The vertical translation follows the analysis in Appendix I. The landing state of the n^{th} cycle can be predicted immediately after $t_{\mathrm{TO}}|_{n-1}$. To do so, we first compute the hopping height h according to the vertical takeoff speed $\dot{z}\left(t_{\mathrm{TO}}\right)|_{n-1}$ from (70). This is

$$h = \left(\frac{2m}{C_d\rho S}\right)\log\left(\sqrt{\left(\frac{C_d\rho S}{2m}\right)\frac{\left(\dot{z}\left(t_{\mathrm{TO}}\right)|_{n-1}\right)^2}{g}+1}\right). \tag{3}$$

Thereafter, the vertical landing speed $\dot{z}\left(t_{\mathrm{LD}}\right)|_{n}$ can be obtained by substituting h from (3) into (68)

$$\dot{z}\left(t_{\mathrm{LD}}\right)|_{n} = -e^{-\frac{C_d\rho S}{2m}h}\sqrt{\frac{2m}{C_d\rho S}g\left(e^{\frac{C_d\rho S}{m}h}-1\right)}. \tag{4}$$

With the estimated hopping height h, the aerial phase time ($t_{\mathrm{asc}}+t_{\mathrm{des}}$) can be obtained by solving (69) and (67),

$$t_{\mathrm{asc}} = \cosh^{-1}\left(e^{-\frac{C_d\rho S}{2m}h}\right)/\sqrt{-\frac{C_d\rho S}{2m}g}, \tag{5}$$

$$t_{\mathrm{des}} = \cosh^{-1}\left(e^{\frac{C_d\rho S}{2m}h}\right)/\sqrt{\frac{C_d\rho S}{2m}g}. \tag{6}$$

Note that in the drag-free scenario, (3) to (6) reduces to

$$h = \left(\dot{z}\left(t_{\mathrm{TO}}\right)|_{n-1}\right)^2/\left(2g\right), \tag{7}$$

$$\dot{z}\left(t_{\mathrm{LD}}\right)|_{n} = \sqrt{2gh} = \dot{z}\left(t_{\mathrm{TO}}\right)|_{n-1}, \tag{8}$$

$$t_{\mathrm{asc}} = t_{\mathrm{des}} = \sqrt{2h/g}. \tag{9}$$

Without considering the air drag in the lateral directions, the lateral velocity remains constant for the entire aerial phase. This results in the lateral landing location of

$$x\left(t_{\mathrm{LD}}\right)|_{n} = x\left(t_{\mathrm{TO}}\right)|_{n-1} + \dot{x}\left(t_{\mathrm{TO}}\right)|_{n}\left(t_{\mathrm{asc}}+t_{\mathrm{des}}\right), \tag{10}$$

$$y\left(t_{\mathrm{LD}}\right)|_{n} = y\left(t_{\mathrm{TO}}\right)|_{n-1} + \dot{y}\left(t_{\mathrm{TO}}\right)|_{n}\left(t_{\mathrm{asc}}+t_{\mathrm{des}}\right), \tag{11}$$

when the ground is assumed level ($z\left(t_{\mathrm{LD}}\right)|_{n} = z\left(t_{\mathrm{TO}}\right)|_{n-1}$). Together, the landing velocity and location of the robot can be fully predicted after the previous takeoff.

C. Stance Phase Dynamics

During the stance phase, the attitude control is disabled [24] and the robot behaves as a point of mass with an axial springy telescopic leg (see Fig. 3(a)). As the stance phase is passive, the subsequent trajectory is determined by the landing velocity $\dot{\mathbf{p}}\left(t_{\mathrm{LD}}\right)$, attitude $\mathbf{R}\left(t_{\mathrm{LD}}\right)$, and the elastomers' preload Δl_{load}. Without slippage, the foot of the robot acts as a free-to-rotate hinge, bringing about a swing motion. We neglected gravity and the thrust to simplify the model as the elastic force f_{e} dominates the dynamics [24]. Particularly for high hops, the elastic force f_{e} can reach up $100mg$ (estimated from leg compression time; see Appendix E). Under these assumptions, the equations of motion reduces to

$$\begin{gathered} m\ddot{\mathbf{p}} = \mathbf{z}_{\mathrm{b}}f_{\mathrm{e}} \quad \text{with} \\ \mathbf{z}_{\mathrm{b}} = \mathbf{R}\mathbf{e}_3 = \left(\mathbf{p}-\mathbf{p}_{\mathrm{foot}}\right)/\left\|\mathbf{p}-\mathbf{p}_{\mathrm{foot}}\right\|, \end{gathered} \tag{12}$$

where $\mathbf{z}_{\mathrm{b}}$ is a unit vector aligned with the leg axis, $\mathbf{p}_{\mathrm{foot}}$ is the location of the foot on the ground (constant for the entire stance phase), $\left\|\mathbf{p}-\mathbf{p}_{\mathrm{foot}}\right\| = l$ denotes the time-varying leg length. Since all forces align with $\mathbf{z}_{\mathrm{b}}$, the angular momentum about $\mathbf{p}_{\mathrm{foot}}$ is conservative. In the stance phase, the robot rotates about the following axis:

$$\mathbf{e}_{\psi} = \left(\mathbf{z}_{\mathrm{b}}\left(t_{\mathrm{LD}}\right)\times\dot{\mathbf{p}}\left(t_{\mathrm{LD}}\right)\right)/\left\|\dot{\mathbf{p}}\left(t_{\mathrm{LD}}\right)\times\mathbf{z}_{\mathrm{b}}\left(t_{\mathrm{LD}}\right)\right\|, \tag{13}$$

as illustrated in Fig. 3(a). Therefore, $\dot{\mathbf{p}}\left(t_{\mathrm{LD}}\right)$, $\dot{\mathbf{p}}\left(t_{\mathrm{TO}}\right)$, $\mathbf{z}_{\mathrm{b}}\left(t_{\mathrm{LD}}\right)$ and $\mathbf{z}_{\mathrm{b}}\left(t_{\mathrm{TO}}\right)$ are coplanar [24] and normal to $\mathbf{e}_{\psi}$. The relationships between the landing state: $\dot{\mathbf{p}}\left(t_{\mathrm{LD}}\right)$, $\mathbf{z}_{\mathrm{b}}\left(t_{\mathrm{LD}}\right)$ and elastomers' preload Δl_{load}, and the takeoff state: $\dot{\mathbf{p}}\left(t_{\mathrm{TO}}\right)$ and $\mathbf{z}_{\mathrm{b}}\left(t_{\mathrm{TO}}\right)$, can be established by an empirical model [43].

We employ θ_{LD}, $\Delta\psi$ and θ_{TO} to describe the angles between velocity and attitude vectors between landing and takeoff (Fig. 3(a)). Here, θ_{LD} is the angle between $-\dot{\mathbf{p}}\left(t_{\mathrm{LD}}\right)$ and $\mathbf{z}_{\mathrm{b}}\left(t_{\mathrm{LD}}\right)$, $\Delta\psi$ is the rotated angle of the body in the stance phase given by the angle between $\mathbf{z}_{\mathrm{b}}\left(t_{\mathrm{LD}}\right)$ and $\mathbf{z}_{\mathrm{b}}\left(t_{\mathrm{TO}}\right)$, and θ_{TO} is the angle between $\mathbf{z}_{\mathrm{b}}\left(t_{\mathrm{TO}}\right)$ and $\dot{\mathbf{p}}\left(t_{\mathrm{TO}}\right)$. The takeoff state, consisting of θ_{TO}, $\Delta\psi$ and takeoff speed $\left\|\dot{\mathbf{p}}\left(t_{\mathrm{TO}}\right)\right\|$ depends on the landing state θ_{LD}, $\left\|\dot{\mathbf{p}}\left(t_{\mathrm{LD}}\right)\right\|$ and Δl_{load}.

Based on findings in [24], angles depicting the takeoff state, $\theta_{\mathrm{LD}}+\Delta\psi$ and $\theta_{\mathrm{LD}}+\Delta\psi+\theta_{\mathrm{TO}}$, are empirically proportional to the landing state θ_{LD}, particularly when θ_{LD} is small. In addition, the takeoff body orientation and velocity ($\Delta\psi$ and θ_{TO}) display little dependence on the landing speed $\left\|\dot{\mathbf{p}}\left(t_{\mathrm{LD}}\right)\right\|$. Hence, they are modeled as

$$\theta_{\mathrm{LD}}+\Delta\psi = k_1\theta_{\mathrm{LD}}, \tag{14}$$

$$\theta_{\mathrm{LD}}+\Delta\psi+\theta_{\mathrm{TO}} = k_2\theta_{\mathrm{LD}}, \tag{15}$$

where k_1 and k_2 are coefficients to be identified experimentally [43]. Compared with the previous model with higher fidelity [24], this model captures the dominant features of the stance dynamics and substantially simplifies the computation.

D. Stance Phase Maps

With the identified coefficients k_1 and k_2, we can predict $\mathbf{z}_{\mathrm{b}}\left(t_{\mathrm{TO}}\right)$ and the direction of $\dot{\mathbf{p}}\left(t_{\mathrm{TO}}\right)$, from the knowledge of the landing state: $\mathbf{z}_{\mathrm{b}}\left(t_{\mathrm{LD}}\right)$ and $\dot{\mathbf{p}}\left(t_{\mathrm{LD}}\right)$. Or we can also predict the direction of landing $\dot{\mathbf{p}}\left(t_{\mathrm{LD}}\right)$ and takeoff velocity $\dot{\mathbf{p}}\left(t_{\mathrm{TO}}\right)$ employing body attitude in stance ($\mathbf{z}_{\mathrm{b}}\left(t_{\mathrm{LD}}\right)$ and $\mathbf{z}_{\mathrm{b}}\left(t_{\mathrm{TO}}\right)$) as detailed below. These predictions are employed in hopping control and state estimation as described below.

1) Takeoff State Prediction: The stance phase map described by (14) and (15) allow us to predict the directions of $\dot{\mathbf{p}}\left(t_{\mathrm{TO}}\right)$ and $\mathbf{z}_{\mathrm{b}}\left(t_{\mathrm{TO}}\right)$ from the landing states. For example, given $\dot{\mathbf{p}}\left(t_{\mathrm{LD}}\right)$ and $\mathbf{z}_{\mathrm{b}}\left(t_{\mathrm{LD}}\right)$, the body rotation direction in the stance phase is obtained in (13). The angular displacement is

$$\Delta\psi = k_1\theta_{\mathrm{LD}} - \theta_{\mathrm{LD}}. \tag{16}$$

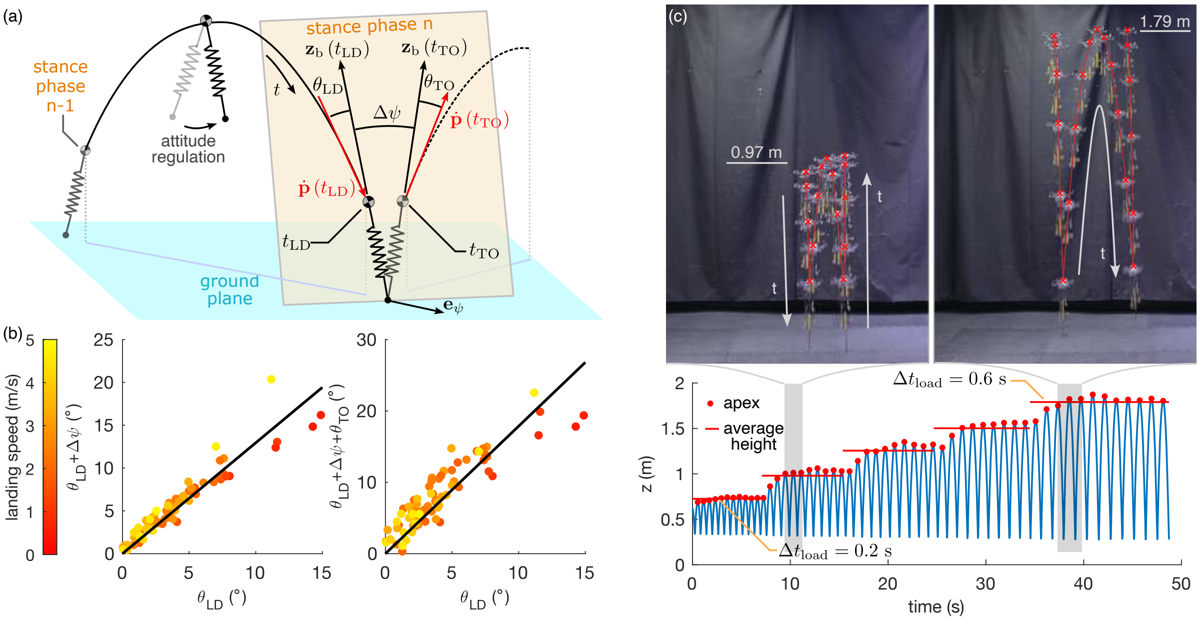

Fig. 3. (a) Diagram illustrating the hopping dynamics. The figure illustrates the relationship between landing velocity, landing attitude, takeoff velocity and takeoff attitude. (b) Parameters identification for the stance phase states mapping. (c) Composite photos and data showing preliminary high-hop tests in the laboratory environment. The robot's positions are shown at 0.12 s intervals. The robot was equipped with 8 rubber bands ($N = 8$).

Therefore, the primary body axis at the takeoff is shifted to

$$\mathbf{z}_\mathrm{b}\left(t_\mathrm{TO}\right) = \mathbf{R}\left(\mathbf{e}_\psi, \Delta\psi\right)\mathbf{z}_\mathrm{b}\left(t_\mathrm{LD}\right), \tag{17}$$

where $\mathbf{R}\left(\mathbf{e}_\psi, \Delta\psi\right)$ is a rotation matrix based on the axis–angle representation. Similarly, the direction of $\dot{\mathbf{p}}\left(t_\mathrm{TO}\right)$ is given by

$$\frac{\dot{\mathbf{p}}\left(t_\mathrm{TO}\right)}{\left\|\dot{\mathbf{p}}\left(t_\mathrm{TO}\right)\right\|} = \mathbf{R}\left(\mathbf{e}_\psi, \Delta\psi + \theta_\mathrm{TO}\right)\mathbf{z}_\mathrm{b}\left(t_\mathrm{LD}\right). \tag{18}$$

The magnitude of $\dot{\mathbf{p}}\left(t_\mathrm{TO}\right)$ cannot be directly predicted from the model as it also dependent on the Δl_load before landing. However, for control purposes in this study, we assume $\left\|\dot{\mathbf{p}}\left(t_\mathrm{TO}\right)\right\| = \left\|\dot{\mathbf{p}}\left(t_\mathrm{LD}\right)\right\|$ for near equilibrium hopping.

2) Desired Landing Attitude: Likewise, (14) and (15) can be employed to find a particular landing attitude to realize a given takeoff direction when the landing velocity is known. Considering the coplanar property of the vectors, $\mathbf{e}_\psi$ can be alternatively computed by

$$\mathbf{e}_\psi = \frac{-\dot{\mathbf{p}}\left(t_\mathrm{LD}\right) \times \dot{\mathbf{p}}\left(t_\mathrm{TO}\right)}{\left\|-\dot{\mathbf{p}}\left(t_\mathrm{LD}\right) \times \dot{\mathbf{p}}\left(t_\mathrm{TO}\right)\right\|}, \tag{19}$$

with $\dot{\mathbf{p}}\left(t_\mathrm{TO}\right)$ being the desired takeoff velocity. Hence, the desired landing attitude is given by

$$\mathbf{z}_\mathrm{b}\left(t_\mathrm{LD}\right) = \mathbf{R}\left(\mathbf{e}_\psi, \theta_\mathrm{LD}\right)\frac{-\dot{\mathbf{p}}\left(t_\mathrm{LD}\right)}{\left\|-\dot{\mathbf{p}}\left(t_\mathrm{LD}\right)\right\|}, \tag{20}$$

where θ_LD is computed based on the angle between $-\dot{\mathbf{p}}\left(t_\mathrm{LD}\right)$ and $\dot{\mathbf{p}}\left(t_\mathrm{TO}\right)$ as

$$\theta_\mathrm{LD} = \left(\theta_\mathrm{LD} + \Delta\psi + \theta_\mathrm{TO}\right)/k_2. \tag{21}$$

3) Landing and Takeoff Directions: Besides, with the knowledge of landing and takeoff attitude vectors, the directions of $\dot{\mathbf{p}}\left(t_\mathrm{LD}\right)$ and $\dot{\mathbf{p}}\left(t_\mathrm{TO}\right)$ can also be obtained

$$\frac{\dot{\mathbf{p}}\left(t_\mathrm{LD}\right)}{\left\|\dot{\mathbf{p}}\left(t_\mathrm{LD}\right)\right\|} = -\mathbf{R}\left(\mathbf{e}_\psi, -\theta_\mathrm{LD}\right)\mathbf{z}_\mathrm{b}\left(t_\mathrm{LD}\right), \tag{22}$$

$$\frac{\dot{\mathbf{p}}\left(t_\mathrm{TO}\right)}{\left\|\dot{\mathbf{p}}\left(t_\mathrm{TO}\right)\right\|} = \mathbf{R}\left(\mathbf{e}_\psi, \Delta\psi + \theta_\mathrm{TO}\right)\mathbf{z}_\mathrm{b}\left(t_\mathrm{LD}\right), \tag{23}$$

where $\theta_\mathrm{LD} = \Delta\psi/\left(k_1 - 1\right)$ and $\theta_\mathrm{TO} = \theta_\mathrm{LD}\left(k_2 - 1\right) - \Delta\psi$ are computed based on (14) and (15). $\mathbf{e}_\psi$ is given by

$$\mathbf{e}_\psi = \frac{\mathbf{z}_\mathrm{b}\left(t_\mathrm{LD}\right) \times \mathbf{z}_\mathrm{b}\left(t_\mathrm{TO}\right)}{\left\|\mathbf{z}_\mathrm{b}\left(t_\mathrm{LD}\right) \times \mathbf{z}_\mathrm{b}\left(t_\mathrm{TO}\right)\right\|}. \tag{24}$$

(22) and (23) are employed for hopping state estimation as detailed below.

V. HOPPING ROBOT CONTROL

The hopping controller is developed based on [24], but customized for leg-actuated hopping. As the aerial phase translational dynamics and the stance phase dynamics are passive, the hopping position control is achieved by regulating the landing attitude of each hop (indexed by n). Based on the stance phase map, the landing attitude determines the takeoff velocity and directs the robot towards the desired landing location in the next step ($n+1$). The controller consists of an open-loop hopping height regulator and a model-based landing position controller as illustrated in Fig. 4.

A. Open-Loop Hopping Height Control

The jump height depends on the interplay between the actuation energy and losses. For near vertical hopping ($\left|\dot{z}\left(t_\mathrm{TO}\right)\right| \gg \left|\dot{x}\right|, \left|\dot{y}\right|$), the height converges to an equilibrium after several hops when the input energy for each cycle is held constant

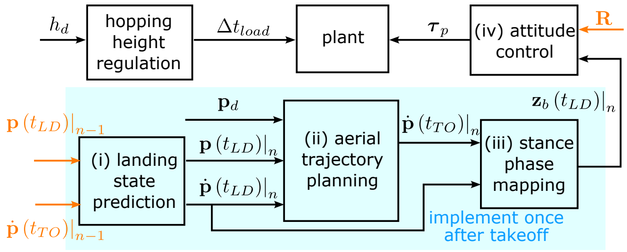

Fig. 4. Block diagram illustrating the hierarchical structure of the hopping controller. The orange signals are feedback either from the model-based hopping state estimator or motion capture system and IMU.

(quantified by Δl_{load}, see (63)). Therefore, the height can be regulated in an open-loop manner.

Based on a linear relationship of the leg actuation time Δt_{load} and leg compression length Δl_{load} (when the winch motor is powered at a fixed voltage, see Fig. S3(a)), we obtain the relationship between leg actuation time Δt_{load} and equilibrium hopping height h_{d}. This strategy allows the hopping height to be controlled without feedback (see Fig. 4 for the structure of the controller).

B. Lateral Position Control

The hopping stabilization and lateral position control are achieved through four sequential steps: (i) landing state prediction, (ii) trajectory planning, (iii) stance phase mapping, and (iv) attitude control (see Fig. 4). The first three steps are executed once per hopping cycle immediately after t_{TO}.

In the first step, the controller predicts the landing location $\mathbf{p}\left(t_{\text{LD}}\right)|_n$ and velocity $\dot{\mathbf{p}}\left(t_{\text{LD}}\right)|_n$ (via (4) to (11)) immediately after the takeoff. This operation neglects the air drag ($C_{\text{d}} = 0$). Next, we plan the trajectory ahead by calculating the landing position for the next cycle $\mathbf{p}\left(t_{\text{LD}}\right)|_{n+1}$ based on the landing location setpoint $\mathbf{p}_{\text{d}}$ and the current estimated landing position $\mathbf{p}\left(t_{\text{LD}}\right)|_n$. The goal is to reduce the position error $\mathbf{p}_{\text{d}} - \mathbf{p}\left(t_{\text{LD}}\right)|_n$ for the next cycle:

$$\mathbf{p}\left(t_{\text{LD}}\right)|_{n+1} = \mathbf{p}\left(t_{\text{LD}}\right)|_n + \xi\left(\mathbf{p}_{\text{d}} - \mathbf{p}\left(t_{\text{LD}}\right)|_n\right), \tag{25}$$

where $\xi \in [0, 1]$ is an incremental gain, governing the convergence rate. As ξ approaches 1, the robot is commanded to jump to $\mathbf{p}_d$ in a single hop, resulting in more aggressive behavior. A lower ξ yields a smaller, conservative step.

Then the desired takeoff velocity $\dot{\mathbf{p}}\left(t_{\text{TO}}\right)|_n$ is determined according to the planned trajectory when a coefficient κ to inhibit over aggressive hopping maneuver as detailed below.

C. Takeoff Velocity and Ballistic Trajectory Planning

The desired takeoff velocity $\dot{\mathbf{p}}\left(t_{\text{TO}}\right)|_n$ is evaluated according to the next landing location $\mathbf{p}\left(t_{\text{LD}}\right)|_{n+1}$. To do so, we assume $\dot{z}\left(t_{\text{TO}}\right) = \|\dot{\mathbf{p}}\left(t_{\text{LD}}\right)\| = \|\dot{\mathbf{p}}\left(t_{\text{TO}}\right)\|$ (near vertical hopping at a constant height). Then, the lateral components of $\dot{\mathbf{p}}\left(t_{\text{TO}}\right)|_n$ is determined from

$$\begin{bmatrix} \dot{x}\left(t_{\text{TO}}\right)|_n & \dot{y}\left(t_{\text{TO}}\right)|_n & 0 \end{bmatrix}^{\text{T}} = \frac{\mathbf{p}\left(t_{\text{LD}}\right)|_{n+1} - \mathbf{p}\left(t_{\text{LD}}\right)|_n}{t_{\text{asc}} + t_{\text{des}}}, \tag{26}$$

$$\text{with} \quad t_{\text{asc}} + t_{\text{des}} = 2\sqrt{2h/g}, \tag{27}$$

is the entire aerial phase time and h is the hopping height estimated from $\left\|\dot{\mathbf{p}}\left(t_{\text{TO}}\right)|_n\right\|^2 / (2g)$.

To satisfy the condition of near vertical hopping, $\dot{x}\left(t_{\text{TO}}\right)|_n$ and $\dot{y}\left(t_{\text{TO}}\right)|_n$ should be notably lower than $\|\dot{\mathbf{p}}\left(t_{\text{LD}}\right)\|$, $\|\dot{\mathbf{p}}\left(t_{\text{TO}}\right)\|$, or $\dot{z}\left(t_{\text{TO}}\right)$. If this is not immediately satisfied from (25), we scale down the lateral components of $\dot{\mathbf{p}}\left(t_{\text{TO}}\right)|_n$ to ensure that

$$\sqrt{\dot{x}\left(t_{\text{TO}}\right)|_n^2 + \dot{y}\left(t_{\text{TO}}\right)|_n^2} / \|\dot{\mathbf{p}}\left(t_{\text{LD}}\right)\| = \kappa \ll 1, \tag{28}$$

where κ is a coefficient that prevents aggressive hopping. Excessively large θ_{LD} or a large lateral leap violates the near-vertical assumption and may degrade control performance.

We employ the map to compute the desired landing attitude $\mathbf{z}_{\text{b}}\left(t_{\text{LD}}\right)|_n$ (see Section IV-D) and command the robot to re-orient its attitude accordingly while it is in the air. The attitude control is implemented using the method outlined in [24]. This control framework is principally similar to the model-based controller [24] but with a simpler implementation.

VI. INERTIA-BASED HOPPING SENSORIMOTOR AUTONOMY

Achieving autonomous hopping is essential for practical deployment of hopping robots, as it enables them to operate in real-world scenarios. Stability is particularly critical because continuous hopping requires precise control of both attitude and touchdown angles to ensure consistent and safe landings. However, very few robots [24], [32], [44], [71] have demonstrated sustained hopping with autonomous control without external stabilization mechanisms. Although there have been a few successful efforts to develop onboard hopping pose estimation for outdoor operations [40], [44], existing techniques are tailored to specific hopping controllers and require additional sensors for leg extension measurement or heavy LiDAR system, limiting their broader applicability.

In this study, we address this challenge using an onboard IMU to estimate both the attitude and velocity of the robot. The primary difficulty stems from the nature of hopping: unlike flying, the robot spends over 95% of its time in free fall [24]. This prevents standard IMU-based attitude estimation, which typically uses a complementary filter [72]: gyroscope readings predict orientation, while accelerometer readings correct the prediction based on gravity sensing. In free fall, gravity cannot be reliably sensed, rendering conventional correction methods ineffective [40]. To overcome this, we replace the accelerometer-based correction with a model-based approach. Specifically, we use a stance-phase dynamic model and assume a ballistic trajectory during the aerial phase. This imposes constraints on the robot's attitude and velocity at both takeoff and landing for consecutive hopping cycles, enabling attitude correction without direct gravity sensing. This correction is performed once per hopping cycle, immediately after takeoff. Lastly, the velocity of the robot can be estimated from the behaviors of the robot in the stance phase, leveraging the stance-phase dynamics. By integrating the estimated velocity, we can determine the robot's cumulative displacement or relative position, enabling trajectory tracking capabilities.

A. Attitude Estimation

The state estimation follows a hierarchical structure and consists of two key stages: prediction and correction stage (see (i) and (ii) in Fig. 5). In the prediction stage, the current attitude estimate is continuously updated based on angular velocity measurements from the gyroscope, integrated at a frequency of 1000 Hz [73]. However, gyroscopic integration alone accumulates drift over time [72], [74]. To correct for this drift, the correction stage applies a model-based adjustment once per hopping cycle. This step aligns the estimated attitude with physical constraints derived from the stance-phase dynamics and ballistic motion, ensuring long-term accuracy. The correction stage is elaborated below. For clarity, we employ an index n to label a hop cycle and superscripts $\cdot^{-}$ and $\cdot^{+}$ to denote quantities before and after the correction.

Starting from the estimated attitudes (represented by rotation matrices) at the moments of landing and takeoff (detected by the acceleration spike and drop), $\mathbf{R}^{-}\left(t_{\mathrm{LD}}\right)|_{n}$ and $\mathbf{R}^{-}\left(t_{\mathrm{TO}}\right)|_{n}$ (enclosing the stance phase), we extract the last row of the rotation matrices as landing and takeoff attitude vectors, represented by $\mathbf{z}_{\mathrm{b}}^{-}\left(t_{\mathrm{LD}}\right)\big|_{n}= \mathbf{R}^{-}\left(t_{\mathrm{LD}}\right)|_{n}\mathbf{e}_3$ and $\mathbf{z}_{\mathrm{b}}^{-}\left(t_{\mathrm{TO}}\right)\big|_{n}= \mathbf{R}^{-}\left(t_{\mathrm{TO}}\right)|_{n}\mathbf{e}_3$. The angular displacement between $\mathbf{z}_{\mathrm{b}}^{-}\left(t_{\mathrm{LD}}\right)\big|_{n}$ and $\mathbf{z}_{\mathrm{b}}^{-}\left(t_{\mathrm{TO}}\right)\big|_{n}$ is converted into swing angle $\Delta\psi$ about the axis

$$\mathbf{e}_{\psi}^{-}=\frac{\mathbf{z}_{\mathrm{b}}^{-}\left(t_{\mathrm{LD}}\right)\times\mathbf{z}_{\mathrm{b}}^{-}\left(t_{\mathrm{TO}}\right)}{\left\|\mathbf{z}_{\mathrm{b}}^{-}\left(t_{\mathrm{LD}}\right)\times\mathbf{z}_{\mathrm{b}}^{-}\left(t_{\mathrm{TO}}\right)\right\|}, \tag{29}$$

as defined in Fig. 3(a).

When the stance phase model is employed ((14) and (15) with empirically identified coefficients k_1 and k_2), we obtain the landing and takeoff angles θ_{LD} and θ_{TO} (see Section IV-D and Fig. 3(a) for the definitions). As a result, the directions of the landing and takeoff velocities (unit vectors) can be computed according to

$$\frac{\dot{\mathbf{p}}^{-}\left(t_{\mathrm{LD}}\right)|_{n}}{\left\|\dot{\mathbf{p}}^{-}\left(t_{\mathrm{LD}}\right)|_{n}\right\|}=\mathbf{R}\left(\mathbf{e}_{\psi}^{-},\theta_{\mathrm{LD}}\right)\mathbf{z}_{\mathrm{b}}^{-}\left(t_{\mathrm{LD}}\right)\big|_{n}, \tag{30}$$

$$\frac{\dot{\mathbf{p}}^{-}\left(t_{\mathrm{TO}}\right)|_{n}}{\left\|\dot{\mathbf{p}}^{-}\left(t_{\mathrm{TO}}\right)|_{n}\right\|}=\mathbf{R}\left(\mathbf{e}_{\psi}^{-},-\theta_{\mathrm{TO}}\right)\mathbf{z}_{\mathrm{b}}^{-}\left(t_{\mathrm{TO}}\right)\big|_{n}, \tag{31}$$

where $\mathbf{R}\left(\mathbf{e}_{\psi}^{-},\cdot\right)$ is a rotation matrix based on the axis-angle representation. These are illustrated in (iii) to (v) in Fig. 5.

The landing velocity direction from the current cycle (n) is then compared with takeoff velocity direction computed in the previous step ($n-1$). Together, they form a base for the ballistic trajectory of the aerial phase (neglecting the air drag) as illustrated in Fig. 6, these two vectors should be coplanar with and symmetric about the gravity direction or $\mathbf{e}_3$. This implies these velocity directions are expected to satisfy

$$\left(\frac{\dot{\mathbf{p}}\left(t_{\mathrm{TO}}\right)|_{n-1}}{\left\|\dot{\mathbf{p}}\left(t_{\mathrm{TO}}\right)|_{n-1}\right\|}-\frac{\dot{\mathbf{p}}\left(t_{\mathrm{LD}}\right)|_{n}}{\left\|\dot{\mathbf{p}}\left(t_{\mathrm{LD}}\right)|_{n}\right\|}\right)\times\mathbf{e}_3=0. \tag{32}$$

We assume the mismatch between the estimated velocity directions from (30) and (31) and the condition described by (32) is attributed to the inaccurate attitude estimate $\mathbf{R}^{-}$.

The attitude correction is achieved by introducing a correction rotation $\mathbf{R}_{\mathrm{C}}$ such that $\mathbf{R}^{+}=\mathbf{R}_{\mathrm{C}}\mathbf{R}^{-}$ to render the corrected landing and takeoff velocity directions consistent with (32). After $\mathbf{R}_{\mathrm{C}}$ is adopted, $\mathbf{z}_{\mathrm{b}}^{+}=\mathbf{R}_{\mathrm{C}}\mathbf{z}_{\mathrm{b}}^{-}$ and the velocity directions from (30) and (31) become

$$\frac{\dot{\mathbf{p}}^{+}\left(t_{\mathrm{LD}}\right)|_{n}}{\left\|\dot{\mathbf{p}}^{+}\left(t_{\mathrm{LD}}\right)|_{n}\right\|}=\mathbf{R}\left(\mathbf{e}_{\psi}^{+},\theta_{\mathrm{LD}}\right)\mathbf{R}_{\mathrm{C}}\,\mathbf{z}_{\mathrm{b}}^{-}\left(t_{\mathrm{LD}}\right)\big|_{n}, \tag{33}$$

$$\frac{\dot{\mathbf{p}}^{+}\left(t_{\mathrm{TO}}\right)|_{n-1}}{\left\|\dot{\mathbf{p}}^{+}\left(t_{\mathrm{TO}}\right)|_{n-1}\right\|}=\mathbf{R}\left(\mathbf{e}_{\psi}^{+},-\theta_{\mathrm{TO}}\right)\mathbf{R}_{\mathrm{C}}\,\mathbf{z}_{\mathrm{b}}^{-}\left(t_{\mathrm{TO}}\right)\big|_{n-1}, \tag{34}$$

in which the rotations $\mathbf{R}\left(\mathbf{e}_{\psi}^{+},\theta_{\mathrm{LD}}\right)$ and $\mathbf{R}\left(\mathbf{e}_{\psi}^{+},-\theta_{\mathrm{TO}}\right)$ reflect the inclusion of $\mathbf{R}_{\mathrm{C}}$. Since θ_{LD} and $-\theta_{\mathrm{TO}}$ are computed from the angular displacement between $\mathbf{z}_{\mathrm{b}}\left(t_{\mathrm{LD}}\right)|_{n}$ and $\mathbf{z}_{\mathrm{b}}\left(t_{\mathrm{TO}}\right)|_{n}$, they are unaffected by the correction. On the other hand, the updated rotational axis $\mathbf{e}_{\psi}^{+}$, computed from $\mathbf{z}_{\mathrm{b}}^{+}\left(t_{\mathrm{LD}}\right)\big|_{n}$ and $\mathbf{z}_{\mathrm{b}}^{+}\left(t_{\mathrm{TO}}\right)\big|_{n-1}$, is given by

$$\begin{aligned}\mathbf{e}_{\psi}^{+}&=\frac{\left(\mathbf{z}_{\mathrm{b}}^{+}\left(t_{\mathrm{LD}}\right)\right)\times\left(\mathbf{z}_{\mathrm{b}}^{+}\left(t_{\mathrm{TO}}\right)\right)}{\left\|\left(\mathbf{z}_{\mathrm{b}}^{+}\left(t_{\mathrm{LD}}\right)\right)\times\left(\mathbf{z}_{\mathrm{b}}^{+}\left(t_{\mathrm{TO}}\right)\right)\right\|}\\&=\frac{\left(\mathbf{R}_{\mathrm{C}}\mathbf{z}_{\mathrm{b}}^{-}\left(t_{\mathrm{LD}}\right)\right)\times\left(\mathbf{R}_{\mathrm{C}}\mathbf{z}_{\mathrm{b}}^{-}\left(t_{\mathrm{TO}}\right)\right)}{\left\|\left(\mathbf{R}_{\mathrm{C}}\mathbf{z}_{\mathrm{b}}^{-}\left(t_{\mathrm{LD}}\right)\right)\times\left(\mathbf{R}_{\mathrm{C}}\mathbf{z}_{\mathrm{b}}^{-}\left(t_{\mathrm{TO}}\right)\right)\right\|}=\mathbf{R}_{\mathrm{C}}\mathbf{e}_{\psi}^{-}.\end{aligned}$$

This implies $\mathbf{R}\left(\mathbf{e}_{\psi}^{+},\cdot\right)$ in (33) and (34) can be rewritten as

$$\mathbf{R}\left(\mathbf{e}_{\psi}^{+},\cdot\right)=\mathbf{R}\left(\mathbf{R}_{\mathrm{C}}\mathbf{e}_{\psi}^{-},\cdot\right)=\mathbf{R}_{\mathrm{C}}\mathbf{R}\left(\mathbf{e}_{\psi}^{-},\cdot\right)\mathbf{R}_{\mathrm{C}}^{\mathrm{T}}. \tag{35}$$

As a result, the corrected velocity directions can be written as

$$\frac{\dot{\mathbf{p}}^{+}\left(t_{\mathrm{LD}}\right)|_{n}}{\left\|\dot{\mathbf{p}}^{+}\left(t_{\mathrm{LD}}\right)|_{n}\right\|}=\mathbf{R}_{\mathrm{C}}\frac{\dot{\mathbf{p}}^{-}\left(t_{\mathrm{LD}}\right)|_{n}}{\left\|\dot{\mathbf{p}}^{-}\left(t_{\mathrm{LD}}\right)|_{n}\right\|}\quad\text{and} \tag{36}$$

$$\frac{\dot{\mathbf{p}}^{+}\left(t_{\mathrm{TO}}\right)|_{n-1}}{\left\|\dot{\mathbf{p}}^{+}\left(t_{\mathrm{TO}}\right)|_{n-1}\right\|}=\mathbf{R}_{\mathrm{C}}\frac{\dot{\mathbf{p}}^{-}\left(t_{\mathrm{TO}}\right)|_{n-1}}{\left\|\dot{\mathbf{p}}^{-}\left(t_{\mathrm{TO}}\right)|_{n-1}\right\|}. \tag{37}$$

The results turn the condition set by (32) to

$$\left(\mathbf{R}_{\mathrm{C}}\left(\frac{\dot{\mathbf{p}}^{-}\left(t_{\mathrm{TO}}\right)|_{n-1}}{\left\|\dot{\mathbf{p}}^{-}\left(t_{\mathrm{TO}}\right)|_{n-1}\right\|}-\frac{\dot{\mathbf{p}}^{-}\left(t_{\mathrm{LD}}\right)|_{n}}{\left\|\dot{\mathbf{p}}^{-}\left(t_{\mathrm{LD}}\right)|_{n}\right\|}\right)\right)\times\mathbf{e}_3=0. \tag{38}$$

The outcome provides two constraints on the correction matrix $\mathbf{R}_{\mathrm{C}}$. In addition to this, we consider the yaw angle or heading direction. Since the stance phase dynamics is independent of the robot's heading angle, we impose another condition on $\mathbf{R}_{\mathrm{C}}$ to ensure that the heading angle is unaltered. To do so, we write $\mathbf{R}_{\mathrm{C}}$ using the axis-angle representation $\mathbf{R}_{\mathrm{C}}=\mathbf{R}\left(\mathbf{e}_{\mathrm{C}},\theta_{\mathrm{C}}\right)$. The heading direction constraint states that r

$$\mathbf{e}_{\mathrm{C}}\cdot\mathbf{e}_3=0. \tag{39}$$

Together, (38) and (39), provide three constraints for $\mathbf{R}_{\mathrm{C}}$. This step corresponds to (vi) in Fig. 5.

Finally, the rotation matrix is updated immediately after each takeoff according to $\mathbf{R}_{\mathrm{C}}$. To improve robustness, the correction is implemented incrementally through a gain $k_c\in[0,1]$: $\mathbf{R}_{\mathrm{C}}\rightarrow\mathbf{R}\left(\mathbf{e}_{\mathrm{C}},k_c\theta_{\mathrm{C}}\right)$, such that

$$\mathbf{R}^{+}=\mathbf{R}\left(\mathbf{e}_{\mathrm{C}},k_c\theta_{\mathrm{C}}\right)\mathbf{R}^{-}.$$

This gain reduces the influence of the correction term, similar to how a complementary filter is employed.

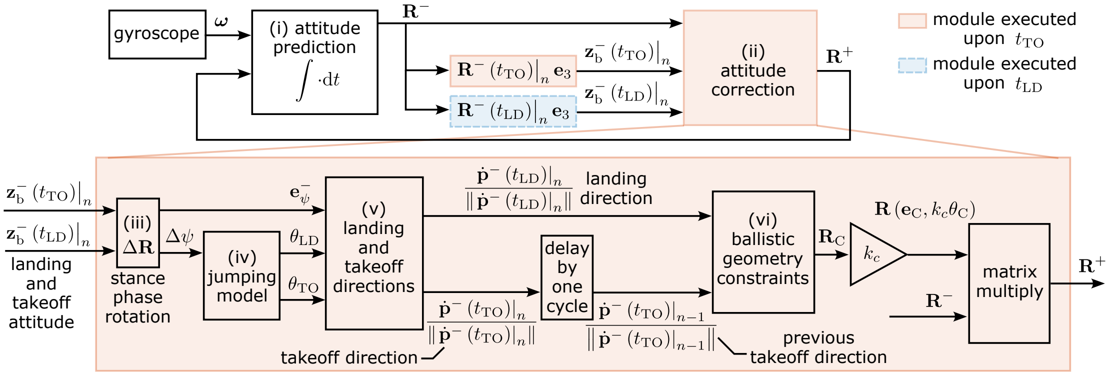

Fig. 5. Block diagram of the model-based attitude estimator. The red and blue parts are executed when the robot takes off and lands.

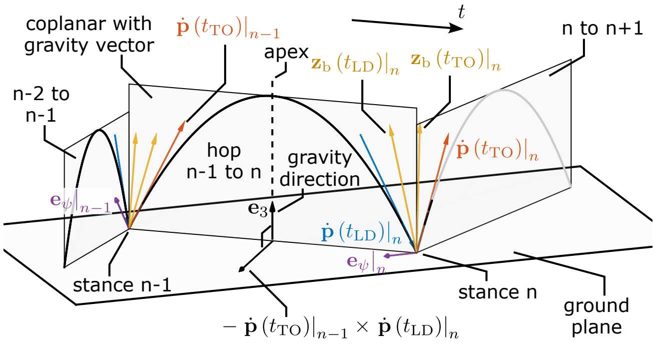

Fig. 6. A diagram illustrating constraints of ballistic trajectories. The takeoff and landing velocities must be coplanar with the vertical axis.

B. Velocity and Position Estimation

Following the attitude correction, the corrected velocity directions are given by

$$\frac{\dot{\mathbf{p}}^{+*}(t_{\mathrm{LD}})|_n}{\|\dot{\mathbf{p}}^{+*}(t_{\mathrm{LD}})|_n\|} = \mathbf{R}(\mathbf{e}_{\mathrm{C}}, k_c\theta_{\mathrm{C}}) \frac{\dot{\mathbf{p}}^-(t_{\mathrm{LD}})|_n}{\|\dot{\mathbf{p}}^-(t_{\mathrm{LD}})|_n\|} \quad \text{and}$$

$$\frac{\dot{\mathbf{p}}^{+*}(t_{\mathrm{TO}})|_n}{\|\dot{\mathbf{p}}^{+*}(t_{\mathrm{TO}})|_n\|} = \mathbf{R}(\mathbf{e}_{\mathrm{C}}, k_c\theta_{\mathrm{C}}) \frac{\dot{\mathbf{p}}^-(t_{\mathrm{TO}})|_{n-1}}{\|\dot{\mathbf{p}}^-(t_{\mathrm{TO}})|_{n-1}\|}.$$

We further estimate the landing speed by evaluating the flight time of the ballistic flight according to

$$\|\dot{\mathbf{p}}^+(t_{\mathrm{LD}})|_n\| = \tag{40}$$

$$\left(\frac{1}{8}g\left(t_{\mathrm{TO}}|_n - t_{\mathrm{LD}}|_{n-1}\right)^2\right) / \left(\mathbf{e}_3^{\mathrm{T}} \cdot \frac{\dot{\mathbf{p}}^+(t_{\mathrm{LD}})|_n}{\|\dot{\mathbf{p}}^+(t_{\mathrm{LD}})|_n\|}\right). \tag{41}$$

And the takeoff speed is assumed equal to the landing speed.

$$\|\dot{\mathbf{p}}^+(t_{\mathrm{TO}})|_n\| = \|\dot{\mathbf{p}}^+(t_{\mathrm{LD}})|_n\|. \tag{42}$$

For position control, we assume the horizontal velocity remains constant for the entire aerial phase. The time integration of the velocity is used to predict the next landing location as illustrated in Fig. 4 (i). This enables the robot to hop and realize a desired trajectory without position feedback.

VII. EXPERIMENT RESULTS

A. Identification and Validation of the Stance Dynamic

We conducted preliminary hopping experiments to identify parameters k_1 and k_2 (from (14) and (15)) and assess the validity of the model. Initially, these parameters were empirically tuned for the hopping controller to achieve relatively stable hopping. Subsequently, the robot was commanded to perform continuous hopping with the varied position and height set by the operator We used the motion capture system for feedback and to record the robot's takeoff and landing states, including $\dot{\mathbf{p}}(t_{\mathrm{LD}})$, $\mathbf{z}_{\mathrm{b}}(t_{\mathrm{LD}})$, $\dot{\mathbf{p}}(t_{\mathrm{TO}})$ and $\mathbf{z}_{\mathrm{b}}(t_{\mathrm{TO}})$. We employed the method in [24] to project them to the best-fitted plane for computing the values of θ_{LD}, $\Delta\psi$, and θ_{TO}. Over the course of a 70-second hopping session, the robot hopped 74 times, covering the landing speeds from 0.44 to 4.89 ms^{-1} and θ_{LD} from 0° to 15°. The parameters were determined using the least squares method as $k_1 = 1.29$ and $k_2 = 1.79$ (Fig. 3(b)). The outcomes affirm that the takeoff state denoted by $\theta_{\mathrm{LD}} + \Delta\psi$ and $\theta_{\mathrm{LD}} + \Delta\psi + \theta_{\mathrm{TO}}$ are primarily dependent on θ_{LD} (irrespective of the landing speed). This confirms the linear models accurately predict the stance phase behavior.

B. Validation of Open-Loop Hopping Height Regulation

We conducted two tests to evaluate the height control strategy. We first equipped 4 rubber bands on the robot and commanded the robot to hop in place and varied the desired height h_{d} from 0.44 to 1.26 m. The motion capture system was used for feedback. The loading time Δt_{load} and loaded length Δl_{load} are 0.15-0.55 s and 13.0-47.5 mm. The results are presented in Fig. S4. It can be seen that, after changing Δt_{load}, the hopping height converged to equilibrium after a few hops, implying the effectiveness of the height control strategy. Compared with the equilibrium hopping model (Fig. S2(a) and (b)), the measured landing speed, takeoff speed and hopping height show good agreement in trend but with a near-constant offset. The root mean square errors (RMSEs) are 0.098 ms^{-1}, 0.112 ms^{-1} and 0.152 m respectively. The errors may be caused by the motor response time that in practice leads to an inaccurate Δt_{load}.

In the second trial, we increased the number of rubber bands to 8 for a preliminary high hop test. During the hop, we gradually increased the Δt_{load} from 0.2 to 0.6 with an interval of 0.1 s. This adjustment increases the hopping height from 0.6 to 1.8 meters as shown in Fig. 3(c) and Movie S3. Each time after Δt_{load} was changed, the hopping height converged to equilibrium within 2-5 hops. When $\Delta t_{\mathrm{load}} = 0.6$ s, the robot settled to a hopping frequency of 0.84 Hz, resulting in

0.59 seconds of unpowered flight per hop. This implies that the robot could potentially jump higher by further increasing Δt_{load}. Limited by space of our motion-capture setup, we conducted tests at higher jump heights in an open environment outside the laboratory (see Section VII-E).

C. Validation of Lateral Position Control

To evaluate control performance, we conducted trajectory-tracking experiments. The motion capture system was used for feedback. We commanded the robot to track a 70-second step trajectory with three steps of sudden changes in the setpoint position. To maintain the jump height, the loading time was set to 0.2 s throughout. The incremental gain ξ of the controller in (25) was set to 0.3 and κ was set to 0.5. These resulted in a conservative hopping behavior such that the robot took multiple steps to reach the new position setpoint as shown in Fig. S5(a) and (b) and Movie S3. This caused a relatively large tracking error when the setpoint position was altered. Consequently, the RMSEs in x and y directions were 0.07 and 0.58 m, with the latter corresponding to the setpoint change. For a stationary setpoint ($t = 0 - 15$ s and $t = 60 - 70$ s), the RMSEs in x and y directions were only 0.049 and 0.060 m.

D. Validation of Inertia-Based Autonomous Hopping

The estimation method enables autonomous hopping control and stabilization when combined with a customized model-based hopping position controller. Using the estimator to provide position, velocity and attitude feedback and motion capture to record ground truth data, we conducted multiple experiments to verify the effectiveness of our approach.

1) Trajectory Tracking: In the 60-second trajectory tracking experiment without any external feedback, the robot performed 145 hops at a consistent height of 0.3 m while realizing a rectangular trajectory (Movie S4, Fig. 7a and b). Compared to ground truth data from a motion capture system (Fig. 7(b), (c) and (d)), we observed the RMSEs of 0.30, 0.40, and 1.80 degrees in estimated roll, pitch, and yaw angles, respectively. The RMSEs for estimated takeoff velocities in x, y and z-direction were 0.16, 0.05 and 0.41 ms^{-1}. The landing positions reconstructed from the onboard estimator closely mirrored the reference, with minor drift from the ground truth. By the end of the experiment, the final position deviated 1.13 m from its starting point after traveling over 6.8 m, corresponding to a position drift rate of only 0.02ms^{-1}.

2) Field Hopping Demonstration: In a more challenging environment, we carried out a field test in an indoor concourse. The robot operated solely on IMU feedback (motion capture system unavailable), with a human operator specifying desired landing locations. The robot traveled approximately 47 m over a three-minute period, successfully navigating uneven terrain and descending two short flights of stairs (Movie S4). We recorded the estimated attitude, horizontal landing positions (reconstructed from onboard estimates), and reference trajectory (Fig. S6). Over 190 s, the attitude estimation remained stable and the robot tracked the reference with a RMSE of 0.47 m. These results demonstrate the reliability and robustness of the estimation and control methods.

To demonstrate the application potential, we mounted a 39-gram camera (Insta360 Go 3s) on the robot to capture onboard video footages (Fig. S7(a)). To accommodate the payload, we slightly shortened the robot's leg to enhance structural rigidity and impact resistance, resulting in a total weight of 95.6 grams, well above the robot's maximum thrust capacity (42 gf). The added mass reduced the hopping height for a given Δl_{load}. With six rubber bands, hopping heights decreased from 0.35 m, 0.74 m, and 1.09 m (without payload) to 0.28 m, 0.52 m, and 0.97 m (with payload) for loading times Δt_{load} of 0.2 s, 0.4 s, and 0.6 s, respectively. The observed trend and reduction in hopping height closely matched model predictions (see Fig. S7(b) and (c)). Although the robot's mass increased by 70% with the camera, the hopping height was reduced by only 20%. This indicates a 36% increase in total system energy while the motor's energy output remained unchanged, attributable to the fact that the added mass did not cause a proportional increase in aerodynamic drag.

Despite carrying the camera, the robot retained stable hoping and demonstrated robust locomotion. The robot successfully hopped up stairs and onto a 50-cm windowsill (see Movie S4 and Fig. 7(e) and (f)). The onboard state estimation and control system effectively preserved stability when encountering changes in ground elevation.

3) Gusts Rejection Test: We also subjected the robot to momentary gusts ranging from 0 to 7.78 ms^{-1}. We used an electric fan to generate wind and an anemometer (Kanomax 6036-AG) to measure the wind speed (Fig. 8(a)). The robot was commanded to hop and retain its position 1.5 to 2 m in front of the fan outlet. While the wind accelerated the positional drift of the estimation to 0.06 ms^{-1}, it did not destabilize the robot (Fig. 8(a), (b) and Movie S5). In an additional outdoor trial, under sustained winds below 4.4 ms^{-1} (by fanning) for more than 40 seconds, the robot's position drifted less than 1.4 meters (measured on-site, see Fig. 8(c) and Movie S5). These results highlight the reliability and robustness of the control and state estimation methods.

4) Comparison with Conventional Attitude Estimators: To benchmark the proposed attitude estimator, we conducted additional tests. In the first trial, the robot hopped in place (fixed positional setpoint) for approximately 40 seconds employing the proposed method. We then disabled the model-based correction step in the estimator, leaving only the integration of gyroscopic readings for attitude estimation, while position and velocity estimation were unchanged. Over the next 23 seconds, the attitude estimation error increased from 0.6° to 1.7°. This gradual rise in attitude error led to accumulating lateral position errors as shown in Fig. S8. Eventually, this drift caused the robot to leave the 3 m × 3 m test arena, resulting in a collision with the wall (Movie S5). Such attitude estimation drift is not unique to the hopping robot. Disabling the attitude correction from the accelerometer reading in a complementary filter on a quadcopter (Bitcraze Crazyflie 2.1) results in a similar attitude drift rate, as shown in Fig. S9.

In the second trial, we repeated the experiment, but upon disabling the estimator, we switched to a standard complementary filter [72]. The robot exhibited similar behavior with comparable position drift as shown in Movie S5. Over 36

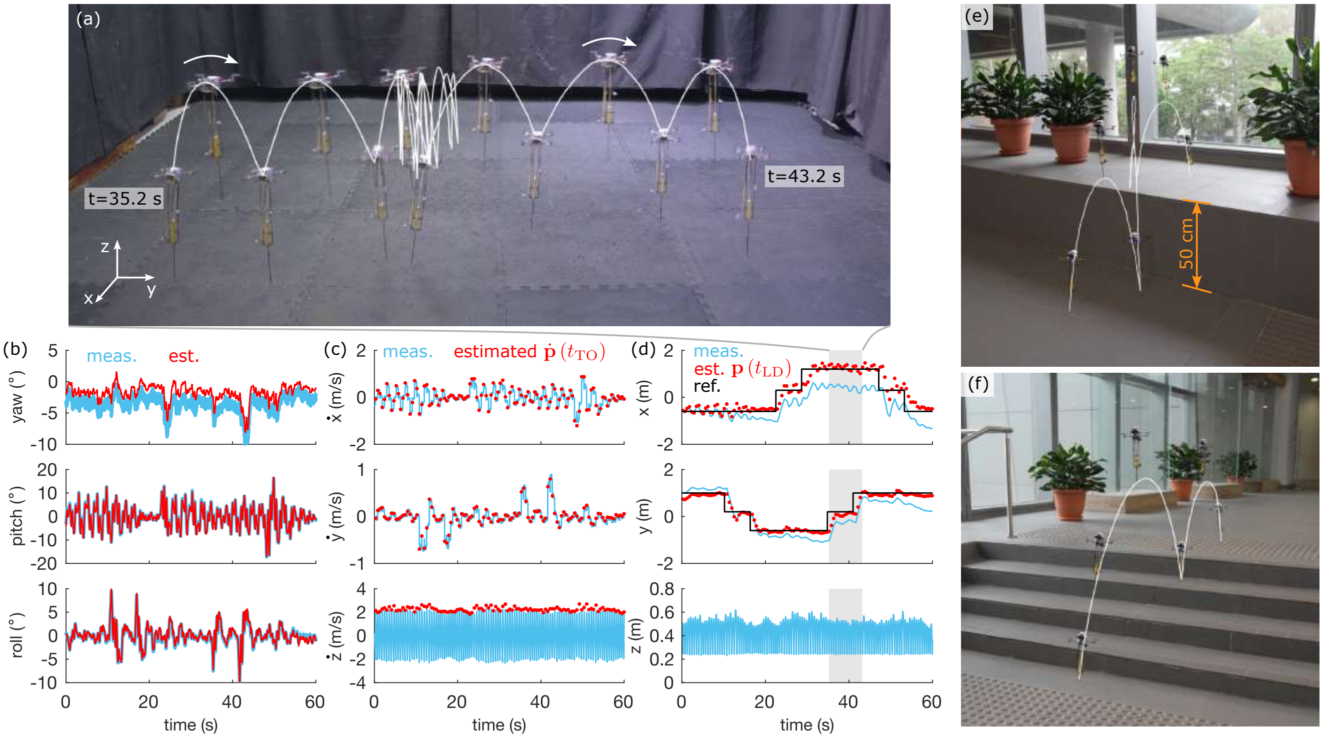

Fig. 7. (a) A composite photo showing the partial trajectory of the robot during the indoor hopping experiment conducted for evaluating the hopping state estimation and control performance. The robot hopped using only the estimator for feedback. The motion capture system was used to record the ground-truth data only.(b) Comparison between estimated body attitude and ground truth in (a). (c) Estimated takeoff velocity versus ground truth in (a). (d) Comparison between estimated landing position, actual trajectory and reference trajectory in (a). (e) and (f) Field hopping demonstration. The robot was commanded to increase its hopping height to jump over four steps of a staircase and onto a 50-cm windowsill.

seconds, the attitude error increased from $1.6°$ to $6.0°$ as shown in Fig. S10. These results demonstrate that, without the proposed method, a hopping robot is unable to maintain long-term drift-free attitude estimation in hopping.

E. High Hop Demonstration

We showcased the robot's high hopping capabilities in an indoor atrium (Fig. 9(a), Movie S6). Without a motion capture system, we employed environmental features serving as reference scales. We positioned the camera 18 m away from the robot for capturing the footage. These measures effectively reduce the impact of perspective and facilitate the hopping height estimation from the videos. During the test, the robot was commanded to gradually increase its leg actuation time up to 1 s, resulting in an increased hopping height and progressively longer intervals between impulses captured by the onboard accelerometer (Fig. 9(b) and (c)). The robot achieved a maximum hopping height of 3.6 m, spending 1.85 s in the aerial phase with an f^* of 0.93 (Fig. 9(a), (b) and Movie S6). High continuity is attribute to the employed high-stiffness elastic elements ($k_e = 0.369\ \mathrm{Nmm}^{-1}$ N/mm, $N = 10$) which leads to a short stance phase (< 60 ms, refer to Appendix H and Fig. S11(a) and Movie S7).

This performance surpasses the high jump records [55] of both human and animal (Macropus rufus) and more than double the achievements of leg-actuated hopping robots [24], [31], [32], [54] (see Fig. 1(a) and Table S2). The hopping height of the thrust-based hopping robot, MultiMo-MHR [54], reached 4 meters but only ascending phase of one hop is presented. The robot consistently achieved jumps at a height of 1.6 meters with an f^* of 0.75, as shown in Fig. 1(a). The relatively low f^* is attributed to midair thrust generation [24].

Notably, the achieved hopping height exceeded our initial predictions of 3.0 m based on hopping equilibrium calculations (Fig. S2(d)). This difference can be explained by the additional upward thrust used for attitude regulation. Accelerometer data showed a consistent upward acceleration averaging 1.26 ms^{-2} throughout the aerial phase (Fig. 9(c)). This additional force increases the robot's energy during ascent and reduces it during descent, resulting in nearly constant total energy at landing and takeoff. The net acceleration experienced by the robot decreased from g to 8.55 ms^{-2} or $0.87g$ (Fig. 9(c)), indicating that aerodynamic thrust for attitude control contributes to $\sim$15% of the maximum height. Unlike thrust-based hopping robots, where thrust was mostly generated in the ascending phase to gain height [24], [43], [54], the thrust here is mainly for attitude control. The accelerations are almost identical in ascending and descending phases.

To better understand the robot's energy efficiency, we analyzed its power consumption based on recorded motor commands (excluding propulsion for attitude stabilization, detailed in Appendix J-A). The maximum total electrical power input was 3.4 W, observed as the robot increased its hopping height to over 2 m (Fig. 9(d)). Of this, only 2.0 W was used to preload the elastomer, which accounts for the mechanical power input to the leg. After factoring in energy

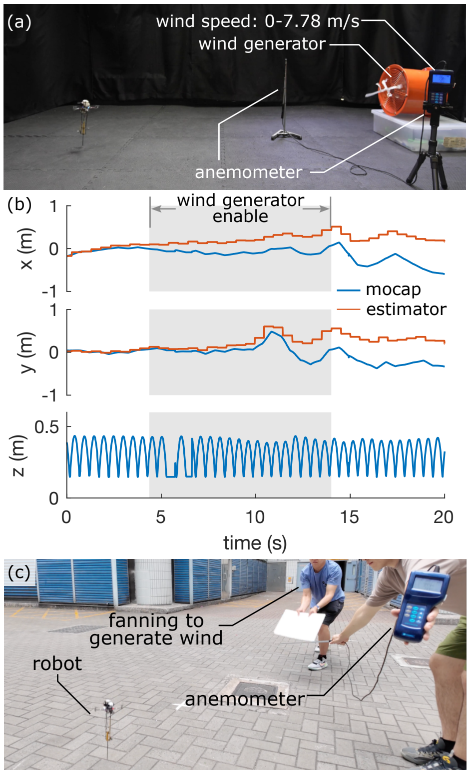

Fig. 8. (a) Photo showing the robot and the experimental setup from the indoor gust rejection test. (b) The estimated position and the ground truth from the indoor test. (c) Photo showing the robot and the setup from the outdoor gust rejection test.

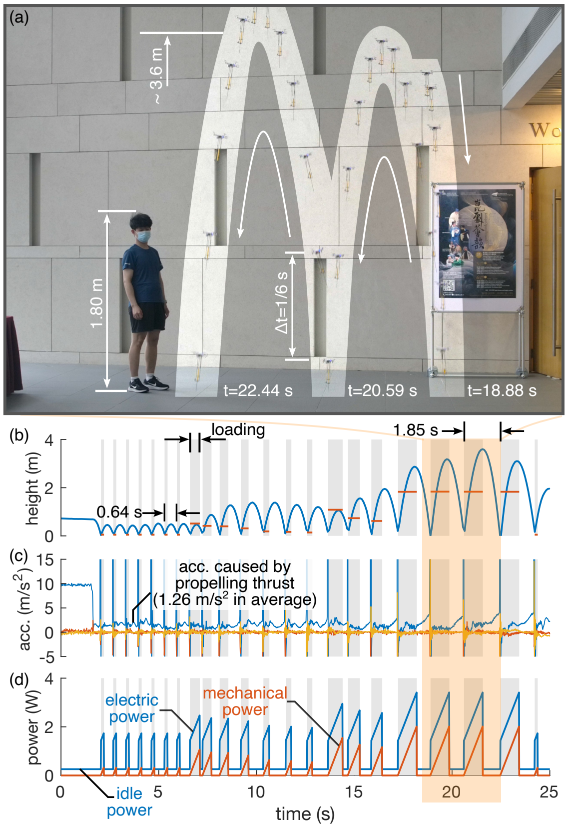

Fig. 9. (a) A composite photo showing the high hop test. The robot reached 3.6 m after several steps. (b) The altitude of the robot (reconstructed from the video, blue line) and the estimated mechanical input energy during each aerial phase presented in terms of height (E/mg, red lines). (c) Readings from the accelerometer. The intervals between impulses (ground contact) correspond to the varying hopping height. (d) Actuation power. The blue and red lines denote the electrical input and mechanical output powers of the leg motor.

losses due to elastic hysteresis, the final energy output by the leg corresponded to a hopping height of 1.83 m, or 51% of the achieved height (Fig. 9(b)). This high energy recovery efficiency played a crucial role in enabling the robot's record-breaking leg-actuated hopping performance.

VIII. Conclusions

The parallel-elastic actuation with reactive latch mechanism introduced herein provides an efficient and powerful power modulation mechanism for hopping. By preloading elastomers in mid-air, the robot can generate high power during the stance phase, without the need for actuators with higher power density. With an ability to reach and adapt to various hopping heights, this advancement has radically elevated robotic hopping performance with broader implications. Given the dynamic similarities between running and hopping, this approach could potentially be applied to bipedal, quadrupedal running robots, or even lower limb exoskeletons, enabling unprecedented running or jumping performance with limited actuator power. However, the mechanism cannot be directly extended to walking or other legged robots that require precise leg contraction control. This limitation arises from the mechanical coupling between the leg contraction and elastomer loading. To overcome this, future designs may decouple the elastomer from the leg contraction mechanism [10].

While the developed robot has demonstrated remarkable hopping capabilities, its low mass-to-surface-area ratio does impose limitations on maximum hopping height, particularly due to air resistance (as detailed in Appendices F and I). Although the actuation mechanism reduces power demands, energy loss remains a challenge (see Fig. 9(d)). The primary sources of energy loss include mechanical friction in the gear transmission, hysteresis in the elastomers, and inefficiencies in the motor. Additionally, the auxiliary elastic elements do not contribute to takeoff, meaning all their stored energy is lost. Future research may focus on reducing energy loss and improving overall efficiency. Another important area for improvement is the robot's ability to recover from falls and initiate jumps from a stationary position. To achieve this, additional mechanical structures or modifications will be needed, which will be an important focus of future development.

Using only an inertial sensor, the proposed state estimation method enables accurate and reliable drift-free attitude estimation and slow-drift position estimation. In contrast, standard sensor fusion methods relying solely on inertial data suffer from estimation drift, limiting the robot to hop stably for only a short period [75] (Section VII-D4 and Movie S5).

Unlike thrust-based hopping robots [24], [53], [54], the reactive parallel-elastic mechanism does not rely on aerodynamic thrusters to replenish energy lost during hopping, requiring less actuation power. For instance, Hopcopter consumed 7.57 W during powered ascents [24], [70], whereas leg actuation in this study required only 1.7 to 3.4 W (power density of 31.5 to 63.0 Wkg^{-1}) (see Fig. 9(b)). The robot's average power was 0.83 W and showed no increasing trend with hopping height (see Appendix J-B). The low average power reflects the minimal power required for thruster-based attitude control as the leg motor remains idle for most of the aerial phase.

By storing energy in the elastomer, the reactive parallel-elastic hopper can achieve a high takeoff speed immediately upon landing, even if the landing speed is low, such as when jumping to a higher position or suddenly increasing hopping height (see Fig. 7(e), (f) and Movie S4). In contrast, thrust-based hopping robots must rely on aerodynamic thrust to gain height, or build up energy over multiple hops [54].

Furthermore, while thrust-based robots employ aerodynamic propulsion for both lift and attitude control, our robot's thrusters are mainly for attitude control. This function could alternatively be achieved using reaction wheels or other inertia-based mechanisms. Such modifications would render the robot suitable for lunar or planetary exploration. In environments without air, conventional aircraft are inoperable, and hopping becomes one of the few locomotion strategies capable of efficiently overcoming high obstacles. In low-gravity situations, the robot can achieve even higher jumps, further enhancing its capability to traverse challenging terrains and obstacles.

APPENDIX A
ACTUATION LIMIT FOR DIRECT-DRIVE JUMPERS

To determine the minimum power requirement, we assume that the actuator sustains the maximum output power $P_{\max}$ throughout the takeoff stroke [56]. The leg actuation force f_{leg} decreases with increasing velocity v as $f_{\text{leg}}v = P_{\max}$. Substituting $f_{\text{leg}} = m\mathrm{d}v/\mathrm{d}t$ yields:

$$v\mathrm{d}v/\mathrm{d}t = P_{\max}/m. \tag{43}$$

Integrating this equation over vertical displacement z, with $\mathrm{d}v/\mathrm{d}t = v\mathrm{d}v/\mathrm{d}z$, gives the takeoff velocity:

$$v_{\text{TO}} = \left(3P_{\max}l_{\text{leg}}/m\right)^{1/3}, \tag{44}$$

where l_{leg} is the leg stroke extension. The resulting maximum jumping height is

$$h_{\max} = \frac{v_{\text{TO}}^2}{2g} = \frac{3^{2/3}}{2g}\left(\frac{P_{\max}l_{\text{leg}}}{m}\right)^{2/3}. \tag{45}$$

Additionally, directly integrating (43) provides the minimum stance phase duration for a given hop height:

$$t_{\text{stance}} = mgh/P_{\max}. \tag{46}$$

Combining the stance phase time and aerial phase time leads to the upper limit of normalized hopping frequency f^* for direct drive jumpers as

$$\begin{aligned} f^* &< \frac{t_{\text{flight}}}{t_{\text{stance}} + t_{\text{flight}}} = \frac{\sqrt{8h/g}}{mgh/P_{\max} + \sqrt{8h/g}.} \\ &= \left(1 + \frac{m}{P_{\max}}g\sqrt{gh/8}\right)^{-1}, \end{aligned} \tag{47}$$

dependent on h and power density $P_{\max}/m$ and independent of l_{leg}. However, due to h is bounded by $h_{\max}$ ((45)), (47) is valid only when $h \leq h_{\max}$.

APPENDIX B
NORMALIZED HOPPING FREQUENCY LIMIT

A. Series-Elastic Jumpers

While there is no height limit for series-elastic jumpers as the mechanical advantage can be designed to prolong the spring loading phase, the extended stance phase reduces the continuity. Therefore, the normalized frequency f^* of series-elastic jumpers is still constrained by the power density in the same manner as direct-drive jumpers. However, the spring permits energy recycling, reducing the time required to replenish the energy. As a result,

$$f^* < \left(1 + \frac{m}{P_{\max}}(1-\eta)g\sqrt{gh/8}\right)^{-1}, \tag{48}$$

where η is the energy recycling efficiency.

B. Parallel-Elastic Jumpers

A parallel-elastic robot with an energy recycling efficiency of η, hopping at a height h, requires the actuator to replenish the energy $(1-\eta)\,mgh$ during the aerial phase only for cases with $f^* = 1$. Since the aerial phase duration is $2\sqrt{2h/g}$, the height limit is given by

$$h_{\max,\text{p}} = \left(\frac{P_{\max}}{m\,(1-\eta)}\right)^2/g^3. \tag{49}$$

APPENDIX C
HOPPING ROBOT DESIGN

The robot combines a quadcopter and a leg mechanism. The quadcopter, as the main body, consists of four 7×16 mm coreless motors (Crazyflie 716, see Table S5) and 20-mm propellers. A controller board (Bitcraze Crazyflie 2.1) functions as both the hopping controller and structural frame for the thrusters (see Fig. 2(a)).

The leg mechanism, rigidly fixed below the body, includes a leg frame, a reactive latch mechanism and a telescopic leg constructed from carbon fiber rods and 3D-printed components (Fig. 2(a)). The leg moves axially along two sets of guide wheels to maintain alignment with the robot's center of mass (CoM) [24]. The leg elastomer, consisting of N rubber bands, pre-stretched beyond their natural length, is hooked between the leg frame and the telescopic leg. We selected rubber bands over metal springs because their hyperelastic properties provide a higher elastic energy density [76], [77], making them suitable for high hops. The elastomer is further elongated when the leg is compressed. The leg has a maximum stroke length of 150 mm, matching the maximum strain capacity of the rubber hands. This results in a total height of 420 mm from the foot to the robot's CoM, as illustrated in Fig. S12. Using a relatively long stroke length efficiently reduces the maximum elastic force and actuation force required, as well as the structural strength needed for high jumps.

A motor-driven winch, parallel to the telescopic leg, loads the elastomer via a cable and functions as the reactive latch mechanism (Fig. 2(a) and Fig. 10(a)). The winch is powered by a 7×20 mm DC coreless motor (Augiimor) with a 1:100 gearbox (N20), driving two gears (module of 0.5, teeth of

16 and 20). The rotating winch winds the cable, pulling the telescopic leg up through a pulley and stretching the leg elastomer (Fig. 2(b)). The mechanical advantage from motor torque to cable pulling force is $125/r_{\mathrm{w}}$, where $r_{\mathrm{w}} = 1.5$ mm is the radius of the winch shaft. This results in the maximum pulling force of over 50 N, 94 times the robot weight. To conserve energy, a ratchet-pawl mechanism on the driving gear (Fig. 10(a) and (c)) allows the robot to maintain the elastomer in its loaded state without actuating the motor.

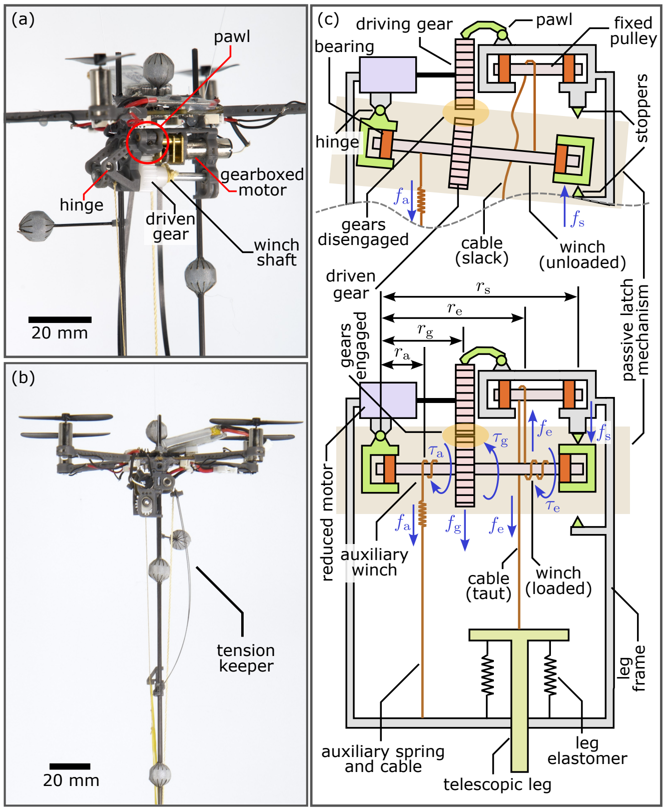

Fig. 10. (a) A close-up photo of the reactive latch mechanism. (b) A side-view photo highlighting the tension keeper. (c) A detailed diagram illustrating the mechanism when the gears are disengaged (top) and engaged (bottom). The diagram includes the auxiliary winch system, but not the pulley for the auxiliary cable and the tension keeper.

The winch shaft incorporates a hinge and two stoppers, enabling it to swing up and down for gear engagement and disengagement, forming the latch mechanism (Fig. 2(b) and (c)). During actuation, the cable tension f_{e}, generated by the leg elastomer, pulls the winch shaft upward, keeping the gears engaged (see Fig. 2(b) and Movie S2). An upper stopper prevents over-rotation and maintains gear backlash (Fig. 10(c)). Upon landing, the leg compresses, further stretching the leg elastomer by Δl_{TS} from Δl_{load} to absorb the landing kinetic energy E_{LD} (Fig. 2(d)). During this phase, the reduction in cable tension allows the hinged winch shaft to swing downward, disengaging the gears via an auxiliary spring. The cable is rapidly unwinded from the winch shaft, assisted by an auxiliary spring and a tension keeper (see Fig. 10(b)), resetting the system. Elastic recoil during the stance phase provides takeoff velocity for the jump, recycling the landing kinetic energy E_{LD} and releasing the preloaded elastic energy E_{load} (Fig. 2(e) and Movie S2).

APPENDIX D
DESIGN CRITERIA OF REACTIVE LATCH

The configuration of the hinged winch shaft, whether the driving gears are engaged depends on the net torque created by tension from the primary and auxiliary cables and the reaction forces from the gears. The balanced condition is described by

$$r_{\mathrm{a}} f_{\mathrm{a}} + r_{\mathrm{g}} f_{\mathrm{g}} - r_{\mathrm{e}} f_{\mathrm{e}} + r_{\mathrm{s}} f_{\mathrm{s}} = 0, \tag{50}$$

where $r_{\mathrm{a}} f_{\mathrm{a}}$ and $-r_{\mathrm{e}} f_{\mathrm{e}}$ represent torques generated by the auxiliary and primary cables with r_{a} and r_{e} being the respective moment arms (see Fig. 10(c)), $r_{\mathrm{g}} f_{\mathrm{g}}$ is the torque induced by the meshed gears, and $r_{\mathrm{s}} f_{\mathrm{s}}$ is the supporting torque generated by the stoppers. The force exerted between two engaged gears f_{g} is a function of their driving torque τ_{g} as

$$f_{\mathrm{g}} = \left(\tau_{\mathrm{g}} \tan \beta_{\mathrm{g}}\right) / r_{\mathrm{gp}}, \tag{51}$$

where $r_{\mathrm{gp}} = 5$ mm is the radius of the gear's pitch circle, and $\beta_{\mathrm{g}} = 20^\circ$ is the pressure angle. Depending on the state of the hinged shaft, the normal force of the stoppers f_{s}, can be either positive (downward) or negative (upward), corresponding to contact between the winch shaft and the top stopper (gears engaged) or the bottom stopper (gears disengaged), respectively (see Fig. 2(b), (c) and Fig. 10(c)). In order for the motor to load the leg elastomer and keep the gears engaged, it is necessary to assure that f_{s} is positive for the entire actuation stroke. According to (50), this is

$$r_{\mathrm{g}} f_{\mathrm{g}} < r_{\mathrm{e}} f_{\mathrm{e}} - r_{\mathrm{a}} f_{\mathrm{a}}. \tag{52}$$

This condition is realized by tuning the axial location of the gear set (r_{g}) and the winches (r_{a} and r_{e}). Modeling the auxiliary spring and the leg elastomer with linear stiffness constants k_{a} and k_{e}, the right-hand side of (52) varies linearly with the angular displacement of the winch shaft θ, offset by the default preload forces: $f_{\mathrm{e},0}$ and $f_{\mathrm{a},0}$, as

$$\begin{aligned} r_{\mathrm{e}} f_{\mathrm{e}} - r_{\mathrm{a}} f_{\mathrm{a}} &= r_{\mathrm{e}} \left(k_{\mathrm{e}} r_{\mathrm{w}} \theta + f_{\mathrm{e},0}\right) - r_{\mathrm{a}} \left(k_{\mathrm{a}} r_{\mathrm{w}} \theta + f_{\mathrm{a},0}\right) & (53) \\ &= r_{\mathrm{w}} \left(r_{\mathrm{e}} k_{\mathrm{e}} - r_{\mathrm{a}} k_{\mathrm{a}}\right) \theta + \left(r_{\mathrm{e}} f_{\mathrm{e},0} - r_{\mathrm{a}} f_{\mathrm{a},0}\right), & (54) \end{aligned}$$

where r_{w} is the radius of the winch shaft.

The left side of (52), $r_{\mathrm{g}} f_{\mathrm{g}}$, is linearly proportional to the driving torque applied on the driven gear τ_{g} (refer to (51)). In equilibrium, the rotational torque is balanced, such that

$$\tau_{\mathrm{g}} = \tau_{\mathrm{a}} + \tau_{\mathrm{e}}. \tag{55}$$

As $\tau_{\mathrm{a}} = f_{\mathrm{a}} r_{\mathrm{w}}$ and $\tau_{\mathrm{e}} = f_{\mathrm{e}} r_{\mathrm{w}}$, τ_{g} is also linearly dependent on θ. That is

$$\tau_{\mathrm{g}} = r_{\mathrm{w}}^2 \left(k_{\mathrm{a}} + k_{\mathrm{e}}\right) \theta + r_{\mathrm{w}} \left(f_{\mathrm{a},0} + f_{\mathrm{e},0}\right). \tag{56}$$

Therefore, by tuning the moment arms (r_{a}, r_{g} and r_{e}) and preload forces ($f_{\mathrm{a},0}$ and $f_{\mathrm{e},0}$) through default preload lengths, we can ensure that (52) is valid for any positive θ.

For the proposed robot, we measured the elastic profiles of the employed elastic elements and computed the stiffness (see Appendix E and Table S4). The gear engagement condition ((52)) was verified when the robot was equipped with 4, 6, 8, and 10 rubber bands as its leg elastomer (see Fig. S13, where $\Delta l = \theta r_{\mathrm{w}}$ is the loaded length).

APPENDIX E
TENSILE TEST

The primary and auxiliary elastic elements were constructed from the same type of rubber bands (diameter: 2 mm and ring radius: 15 mm). For the primary elastic element, N rubber bands were adopted, resulting in an spring constant of $k_e = Nk_{e1}$, where k_{e1} is the constant belonging to a single band. In contrast, the auxiliary elastic element was made from a cut rubber band. This doubles the length and quarters the constant, $k_a = k_{e1}/4$. To evaluate k_{e1}, we measured the force profiles for two and four bundled rubber bands ($N = 2$ and 4).

The tensile test platform consisted of a linear motorized stage and a force/torque sensor (ATI Nano 25, see Fig. S14). The stage stretched the rubber bands and recorded the restoring force (resolution: $1/132$ N after taking into account an amplification from a 10-cm moment arm). In each test, the rubber bands were incrementally stretched from 0 to 72 mm, in intervals of 4 mm, yielding 18 data points per test, as shown in Fig. S15(a). The least squares method identified k_{e1} as 36.9 mN/mm with a coefficient of determination of 0.95.

In this work, the proposed robot supports configurations with $N = 4$ to 12. Adding bands increases the attainable peak jump height, but also results in larger impressive loads on the structure. Therefore, we select N for each experiment based on the required jump height to avoid damage.

APPENDIX F
HOPPING CYCLE AND EQUILIBRIUM HOPPING

The robot achieves continuous jumping by periodically loading the leg elastomer in the aerial phases (see Fig. 2(d)). After t_{TO}, the motor loads the elastomer for a duration Δt_{load}, elongating it by Δl_{load} from the unloaded state , storing energy of E_{load}. Upon t_{LD}, ground impact further compresses the leg, stretching the elastomer to $\Delta l_{\mathrm{load}} + \Delta l_{\mathrm{TS}}$ and absorbing the landing kinetic energy E_{LD} (Fig. 2(d)). The subsequent elastic recoil provides takeoff velocity for the jump, recycling the stored elastic energy.

The takeoff kinetic energy E_{TO} is less than the total stored energy $E_{\mathrm{load}} + E_{\mathrm{LD}}$ due to elastic hysteresis and friction [24]. This loss can be modeled by introducing a constant friction f_c to the leg elastomer model [24]:

$$f_{\mathrm{e}} = k_{\mathrm{e}}\Delta l + \begin{cases} \operatorname{sgn}\left(\Delta \dot{l}\right) f_{\mathrm{c}} & \text{stance} \\ 0 & \text{aerial} \end{cases}, \tag{57}$$

where k_{e} is the elastic constant, Δl denotes the elastomer elongation, and $\Delta \dot{l}$ is strain rate. The loading and unloading of the elastomer can be divided into three phases: (i) low-strain-rate preload in midair (red line in Fig. 2(d)), (ii) high-strain-rate downstroke upon landing, and (iii) high-strain-rate recoil (blue and cyan lines in Fig. 2(d)).

In phase (i), as described by (57), the motor slowly loads the leg elastomer from $\Delta l = 0$ to Δl_{load} (Fig. S15(b), red path). The energy stored prior to landing is

$$E_{\mathrm{load}} = {}^{1}\!/_{2} k_{\mathrm{e}} \Delta l_{\mathrm{load}}^{2}, \tag{58}$$

corresponding to areas 3 and 4 in Fig. S15(b). We assume that the default preload $l_{\mathrm{e},0}$ is negligible compared to the terminal elongation ($\Delta l_{\mathrm{load}} \gg l_{\mathrm{e},0}$).

In phase (ii), after t_{LD}, the elastomer is further compressed by Δl_{TS} (Fig. S15(b), blue path). The elastic force abruptly increases due to the friction f_{c}. The energy absorbed is

$$E_{\mathrm{LD}} = \frac{1}{2}\Delta l_{\mathrm{TS}}\left(2k_{\mathrm{e}}\Delta l_{\mathrm{load}} + 2f_{\mathrm{c}} + k_{\mathrm{e}}\Delta l_{\mathrm{TS}}\right), \tag{59}$$

corresponding to areas 1, 2 and 5 in Fig. S15(b).

Finally, in phase (iii), the elastic recoil accelerates the robot towards takeoff (cyan path in Fig. S15(b)). The parasitic force leads to hysteresis, reducing the elastic force by f_{c}. The loss is captured by areas 1, 2 and 3 in Fig. S15(b). The kinetic energy at takeoff, corresponding to areas 4 and 5 in Fig. S15(b), is

$$E_{\mathrm{TO}} = \frac{1}{2}\left(\Delta l_{\mathrm{load}} + \Delta l_{\mathrm{TS}} - \frac{f_{\mathrm{c}}}{k_{\mathrm{e}}}\right)\left(k_{\mathrm{e}}\left(\Delta l_{\mathrm{load}} + \Delta l_{\mathrm{TS}}\right) - f_{\mathrm{c}}\right), \tag{60}$$

where $\Delta l_{\mathrm{load}} + \Delta l_{\mathrm{TS}}$ is the maximum compression. The ground compression Δl_{TS} can be expressed as a function of Δl_{load} and E_{LD} by solving (59):

$$\Delta l_{\mathrm{TS}} = -\frac{f_{\mathrm{c}}}{k_{\mathrm{e}}} - \Delta l_{\mathrm{load}} + \frac{1}{k_{\mathrm{e}}}\sqrt{\left(f_{\mathrm{c}} + k_{\mathrm{e}}\Delta l_{\mathrm{load}}\right)^{2} + 2k_{\mathrm{e}}E_{\mathrm{LD}}}. \tag{61}$$

With (60), the model predicts the kinetic energy at takeoff E_{TO} and energy losses $E_{\mathrm{load}} + E_{\mathrm{LD}} - E_{\mathrm{TO}}$. The model relates the takeoff speed, landing speed, Δl_{load} and Δl_{TS} as shown in Fig. S16(a) and (b). The model parameters, k_{e} and f_{c} (Table S4), were experimentally identified (see Appendix E and Appendix G and Movie S7).

In continuous vertical hopping, cyclic equilibrium occurs when the loaded energy E_{load} is just sufficient for the robot to reach the previous height h. To account for air drag, we employ a quadratic drag model [69], [70], [78] to capture the vertical hopping dynamics

$$\ddot{z} = -g - \frac{1}{2m}C_{\mathrm{d}}\rho S\left|\dot{z}\right|\dot{z}, \tag{62}$$

where z is the robot's altitude, C_{d} is the drag coefficient, ρ is air density, S is the robot's effective aerodynamic area. With the boundary condition $\dot{z}\left(t_{\mathrm{apx}}\right) = 0$, ($t_{\mathrm{apx}}$ is the time at the apex), we analytically solve $\dot{z}\left(t\right)$ for descending and ascending trajectories. The equilibrium landing and takeoff speeds (v_{LD} and v_{TO}) as functions of h are given by (68) and (70) as detailed in Appendix I. Fig. S2(a) shows v_{LD} and v_{TO} under different lumped drag coefficient. By experimentally dropping the robot from 10 different heights (0.12–1.0 m) and measuring the landing velocities, we identified the drag coefficient. The best-fit value of $\frac{1}{2m}C_{\mathrm{d}}\rho S$ is $0.1\ \mathrm{m}^{-1}$ (see Fig. S2(a)). This coefficient yields an RMSE of 0.10 m/s for landing-speed prediction on the test data (see Fig. S17).

To sustain equilibrium hopping at height h, the loaded energy must compensate for frictional losses and provide additional energy $\frac{1}{2}m\left(v_{\mathrm{TO}}^{2}\left(h\right) - v_{\mathrm{LD}}^{2}\left(h\right)\right)$ to overcome air drag. The required loaded length Δl_{load} can be found by solving (60) and (61). Substituting E_{TO} and E_{LD} by $\frac{1}{2}mv_{\mathrm{TO}}^{2}\left(h\right)$ and $\frac{1}{2}mv_{\mathrm{LD}}^{2}\left(h\right)$ using (68) and (70) (Appendix I), the equilibrium hopping height (h) can be expressed as a function of Δl_{load} (Fig. S2(b)) and is given by

$$h\left(\Delta l_{\mathrm{load}}\right) = -\frac{2m}{C_{\mathrm{d}}\rho S}\log\sqrt{\frac{g}{g+\frac{1}{2m}C_{\mathrm{d}}\rho S v_{\mathrm{TO}}^{2}\Delta l_{\mathrm{load}}}}. \quad (63)$$

The models accounting for and neglecting drag reveal a notable difference in h, particularly for $h > 1$ m, indicating substantial loss due to drag in high hops. In experiments (the robot was equipped with 4 rubber hands), the drag-inclusive model accurately predicted h, v_{TO} and v_{LD} in the passive hopping height regulation experiments (see Fig. S2(a) and (b)), with RMSEs of 0.152 m, 0.098 ms^{-1}, and 0.112 ms^{-1}.

The leg model also predicts the corresponding total elongation of the elastomer $\Delta l_{\mathrm{load}} + \Delta l_{\mathrm{TS}}$ (Fig. S2(c)). Assuming the friction f_{c} is proportional to the number of rubber bands N, the maximum hopping height of the robot is attained when $\Delta l_{\mathrm{load}} + \Delta l_{\mathrm{TS}}$ reaches the maximum stroke length (15 cm). The height limit increases with N but at a diminishing rate due to the growing dissipation from air drag at higher hops.

The required actuator power for a given equilibrium hopping height can be predicted by evaluating the aerial phase duration and the energy cost of loading the elastomer. Based on the aerial trajectory described by (62), the flight time is computed using (67) and (69) (Appendix I). The energy loaded into the leg elastomer is given by (58). The theoretical power requirement for a particular hopping height is

$$P = E_{\mathrm{load}}g/\left(t_{\mathrm{des}} + t_{\mathrm{asc}}\right), \quad (64)$$

as shown in Fig. S2(d). In the absence of drag, (64) is lower bounded by $gf_{\mathrm{c}}/\sqrt{k_{\mathrm{e}}}$. This contradicts the derivation in Fig. 1(d), where energy loss is attributed to a constant friction force, resulting in a non-constant leg efficiency (η). When air drag is considered, the required power increases with the hopping height, but with a decreasing gradient, indicating air drag becomes more dominant in high hops.

Additionally, the model predicts that adding more rubber bands increases the power requirement. This is because of the potentially higher dissipation in elastomer (modeled as friction, f_{c}). When taking these issues into consideration, we can predict the maximum hopping height of the robot is 3.02 m when it is equipped with 10 rubber bands, this balancing the hopping height and power requirements (see Fig. S2(d)).

APPENDIX G
CHARACTERIZATION OF LEG MECHANISM

The leg model is subject to physical and design parameters, including k_{e} and f_{c}. The total stiffness $k_{\mathrm{e}} = Nk_{\mathrm{e1}}$ is characterized through tensile tests (see Appendix E). The constant friction force f_{c} presents at high strain rates and is difficult to measure directly. Instead, we identified f_{c} by comparing predicted takeoff speeds with experimental observations.

To estimate f_{c}, we solve for the minimum RMSE of takeoff velocity ($\hat{v}_{\mathrm{TO}}(f_{\mathrm{c}}) - v_{\mathrm{TO}}$) over the 28 drop tests (see Appendix H), where $\hat{v}_{\mathrm{TO}} = \sqrt{2E_{\mathrm{TO}}/m}$ is the predicted takeoff velocity subject to $E_{\mathrm{LD}} = \frac{1}{2}mv_{\mathrm{LD}}^{2}$ and Δl_{load}. The best-fit parameter is $f_{\mathrm{c}} = 0.818$ N (Fig. S16(a)). The RMSE is 0.10 m/s. The model also accurately predicted that the maximum leg contractions which are solely dependent on their v_{LD} as shown in Fig. S16(b), with the RMSE of 3.5 mm.

APPENDIX H
DROP TESTS

The setup of the drop tests follows the study [24]. We employed a programmed gripper to suspend the robot in an upright orientation and loaded the leg elastomer by Δl_{load} prior to release. Once triggered, the gripper released the robot. A high-speed camera (MotionBLITZ EoSens mini 2) captured the landing and takeoff sequences at 1685 frames per second. By tracking features in the video (Kanade-Lucas-Tomasi tracker [79]), we reconstructed the trajectories of the robot to measure the landing and takeoff velocities, as well as the elastomer deformation (see Movie S7).

The robot, with four rubber bands ($N = 4$), was dropped from three heights: 0.33, 0.60 and 0.75 m. For each height, we conducted 8-11 drops with varied Δl_{load} ranging from 0 to 75.5 mm, totaling 28 tests. The tests yielded landing speeds v_{LD} ranging from 2.49 to 3.99 m/s, takeoff speeds v_{TO} from 2.06 to 5.19 m/s, and maximum leg contractions $\Delta l_{\mathrm{load}} + \Delta l_{\mathrm{TS}}$ from 39.3 to 103.1 mm, see Fig. S11(a) and (b).

APPENDIX I
EFFECTS OF AIR DRAG

To determine the landing speed $\dot{z}\left(t_{\mathrm{LD}}\right)$ from an apex at height h, taking into account an influence of air drag, we obtain an analytical expression of $\dot{z}\left(t\right)$ from the (62) with the boundary condition of $\dot{z}\left(t_{\mathrm{apx}}\right) = 0$ (t_{apx} is the timestamp when the robot reaches the apex of the trajectory):

$$\dot{z}\left(t\right) = -\sqrt{\frac{2mg}{C_{d}\rho S}}\tanh\left(\sqrt{\frac{1}{2m}gC_{d}\rho S}\left(t - t_{\mathrm{apx}}\right)\right), \quad (65)$$

where C_{d} is the drag coefficient, ρ is air density, S is the robot's effective aerodynamic area. Integrating both sides of the equation from t_{apx} to landing

$$t_{\mathrm{apx}} + t_{\mathrm{des}} = t_{\mathrm{LD}}, \quad (66)$$

we relates the hopping height h with the descent time t_{des}:

$$h = \frac{2m}{C_{d}\rho S}\log\left(\cosh\left(\sqrt{\frac{1}{2m}gC_{d}\rho S}t_{\mathrm{des}}\right)\right). \quad (67)$$

Combining this with (65) and (66) eliminate t_{des}, we maps the landing speed v_{LD} to the hopping height:

$$\dot{z}\left(t_{\mathrm{LD}}\right) = v_{\mathrm{LD}}\left(h\right) = \sqrt{\frac{2mg}{C_{d}\rho S}\left(e^{-2hC_{d}\rho S/m} - 1\right)}. \quad (68)$$

Likewise, the relationship between the hopping height and the takeoff speed is obtained by first solving the equation of motion from the takeoff state

$$h = -\frac{2m}{C_{d}\rho S}\log\left(\cosh\left(\sqrt{-C_{\mathrm{D}}g}t_{\mathrm{asc}}\right)\right), \quad (69)$$

where, $t_{\mathrm{asc}} = t_{\mathrm{apx}} - t_{\mathrm{TO}}$ is the ascending time. Finally, we obtain the relation between height and takeoff speed v_{TO} as

$$\dot{z}\left(t_{\mathrm{TO}}\right) = v_{\mathrm{TO}}\left(h\right) = \sqrt{\frac{2mg}{C_{\mathrm{d}}\rho S}\left(e^{\rho SC_{\mathrm{D}}h/m} - 1\right)}. \quad (70)$$

This indicates that, for a given height h, a robot with a higher ratio of m/S requires a lower takeoff velocity, since it is less susceptible to the air drag and vice versa.

APPENDIX J
POWER MEASUREMENTS

A. Leg Motor Power Measurement and Estimation

We conducted hardware-in-the-loop measurements to evaluate the power required for the leg motor (excluding the thrusters). The setup was designed to record the current and voltage consumed by the robot when the leg motor was powered to load the elastomer with the maximum speed for one second. The current (measured by a current sensor, HW-872A, range: 5 A) and the battery voltage were digitized (National Instruments, PCI-6259) at 1000 Hz. In addition, a camera visually recorded the leg compression. The experiments were carried out with 4, 6, 8 and 10 rubber bands equipped. For each configuration, three repeated trials were carried out. This resulted in 12 tests in total as shown in Fig. S3.

The leg compression speeds displayed little variation as shown in Fig. S3(a) (the averaged speeds are computed using data from 0.1 to 0.9 s). During loading, the battery voltage decreases and the current increases. The entire required power grew with the number of rubber bands. The peak power (averaged over three trials) for N =4, 6, 8 and 10 are 2.66, 3.04, 3.54 and 4.04 W (excluding the power spikes at the beginning) as shown in Fig. S3(b), (c) and (d).

The measured power can be employed to estimate the real-time leg motor power consumption of the robot during hopping. This is achieved by abstracting the power as a function of time, when the motor is powered with its maximum speed. Besides, we also averaged the power when idle, as the idle power of the entire leg system. The best-fitted linear models are shown in Fig. S3(d). These results are employed to estimate the power consumption of the leg motor in high hop demonstration as shown in Fig. 9(d).

B. Power Consumption of the Entire Robot

To measure the total power consumption, a current-sensing module incorporating a Hall-effect sensor (ACS712, 5A) was mounted on the robot alongside a dedicated battery and a 5V DC regulator. The module weighs 8.6 g (see Fig. S18). Combined with the Crazyflie's built-in voltage measurement, this setup enabled real-time power monitoring.

We measured average and peak power consumption across six hopping experiments with $N = 4$, covering jump heights from 0.2 to 1.0 m (Fig. S19 and Fig. S20). The average power was 0.83±0.03 W without an increasing trend with hopping height. The peak power ranged from 2.1 to 2.7 W, substantially higher than the average power due to the motor-startup current spike on top of the power consumed by the thrusters.

REFERENCES

[1] K. N. Webster and T. J. Dawson, "Is the energetics of mammalian hopping locomotion advantageous in arid environments?" *Australian Mammalogy*, vol. 26, no. 2, pp. 153–160, 2004.

[2] C. P. McGowan and C. E. Collins, "Why do mammals hop? understanding the ecology, biomechanics and evolution of bipedal hopping," *Journal of Experimental Biology*, vol. 221, no. 12, p. jeb161661, 2018.

[3] E. Hall-Crags, "An analysis of the jump of the lesser galago (galago senegalensis)," in *Proceedings of the Zoological Society of London*, vol. 147, no. 1. Wiley Online Library, 1965, pp. 20–29.

[4] M. Djawdan and T. Garland Jr, "Maximal running speeds of bipedal and quadrupedal rodents," *Journal of Mammalogy*, vol. 69, no. 4, pp. 765–772, 1988.

[5] L. H. Thornton, T. J. Dick, M. B. Bennett, and C. J. Clemente, "Understanding australia's unique hopping species: a comparative review of the musculoskeletal system and locomotor biomechanics in macropodoidea," *Australian Journal of Zoology*, vol. 69, no. 4, pp. 136–157, 2022.

[6] T. J. Dawson and C. R. Taylor, "Energetic cost of locomotion in kangaroos," *Nature*, vol. 246, no. 5431, pp. 313–314, 1973.

[7] M. Djawdan, "Locomotor performance of bipedal and quadrupedal heteromyid rodents," *Functional Ecology*, pp. 195–202, 1993.

[8] R. Kram and T. J. Dawson, "Energetics and biomechanics of locomotion by red kangaroos (macropus rufus)," *Comparative Biochemistry and Physiology Part B: Biochemistry and Molecular Biology*, vol. 120, no. 1, pp. 41–49, 1998.

[9] T. J. Dawson, *Kangaroos: biology of the largest marsupials*. Cornell University Press, 1995.

[10] S.-H. Chae, S.-M. Baek, J. Lee, and K.-J. Cho, "Agile and energy-efficient jumping–crawling robot through rapid transition of locomotion and enhanced jumping height adjustment," *IEEE/ASME Transactions on Mechatronics*, vol. 27, no. 6, pp. 5890–5901, 2022.

[11] Z. Zhakypov, K. Mori, K. Hosoda, and J. Paik, "Designing minimal and scalable insect-inspired multi-locomotion millirobots," *Nature*, vol. 571, no. 7765, pp. 381–386, 2019.

[12] J.-S. Koh, E. Yang, G.-P. Jung, S.-P. Jung, J. H. Son, S.-I. Lee, P. G. Jablonski, R. J. Wood, H.-Y. Kim, and K.-J. Cho, "Jumping on water: Surface tension–dominated jumping of water striders and robotic insects," *Science*, vol. 349, no. 6247, pp. 517–521, 2015.

[13] M. Noh, S.-W. Kim, S. An, J.-S. Koh, and K.-J. Cho, "Flea-inspired catapult mechanism for miniature jumping robots," *IEEE transactions on robotics*, vol. 28, no. 5, pp. 1007–1018, 2012.

[14] S. Divi, R. S. Pierre, H. M. Foong, and S. Bergbreiter, "Controlling jumps through latches in small jumping robots," *Bioinspiration & Biomimetics*, vol. 18, no. 6, p. 066003, 2023.

[15] S. Divi, J. Yim, M. Bedillion, and S. Bergbreiter, "A programmable substrate to study robots jumping from non-rigid surfaces," *IEEE Robotics and Automation Letters*, 2024.

[16] E. W. Hawkes, C. Xiao, R.-A. Peloquin, C. Keeley, M. R. Begley, M. T. Pope, and G. Niemeyer, "Engineered jumpers overcome biological limits via work multiplication," *Nature*, vol. 604, no. 7907, pp. 657–661, 2022.

[17] V. Zaitsev, O. Gvirsman, U. B. Hanan, A. Weiss, A. Ayali, and G. Kosa, "A locust-inspired miniature jumping robot," *Bioinspiration & biomimetics*, vol. 10, no. 6, p. 066012, 2015.

[18] G.-P. Jung, C. S. Casarez, S.-P. Jung, R. S. Fearing, and K.-J. Cho, "An integrated jumping-crawling robot using height-adjustable jumping module," in *2016 IEEE International Conference on Robotics and Automation (ICRA)*. IEEE, 2016, pp. 4680–4685.

[19] M. A. Woodward and M. Sitti, "Multimo-bat: A biologically inspired integrated jumping–gliding robot," *The International Journal of Robotics Research*, vol. 33, no. 12, pp. 1511–1529, 2014.

[20] M. Kovač, M. Schlegel, J.-C. Zufferey, and D. Floreano, "Steerable miniature jumping robot," *Autonomous Robots*, vol. 28, pp. 295–306, 2010.

[21] M. Kovac, M. Fuchs, A. Guignard, J.-C. Zufferey, and D. Floreano, "A miniature 7g jumping robot," in *2008 IEEE International Conference on Robotics and Automation*. IEEE, 2008, pp. 373–378.

[22] J. An, T. Chung, C. H. D. Lo, C. Ma, X. Chu, and K. S. Au, "Development of a bipedal hopping robot with morphable inertial tail for agile locomotion," in *2020 8th IEEE RAS/EMBS International Conference for Biomedical Robotics and Biomechatronics (BioRob)*. IEEE, 2020, pp. 132–139.

[23] J. Yim, *Hopping Control and Estimation for a High-performance Monopedal Robot, Salto-1P*. University of California, Berkeley, 2020.

[24] S. Bai, Q. Pan, R. Ding, H. Jia, Z. Yang, and P. Chirarattananon, "An agile monopedal hopping quadcopter with synergistic hybrid locomotion," *Science Robotics*, vol. 9, no. 89, p. eadi8912, 2024.

[25] S. Kalouche, "Design for 3d agility and virtual compliance using proprioceptive force control in dynamic legged robots," Ph.D. dissertation, School of Computer Science., Carnegie Mellon Univ. Pittsburgh, PA, 2016.

[26] ——, "Goat: A legged robot with 3d agility and virtual compliance," in *2017 IEEE/RSJ International Conference on Intelligent Robots and Systems (IROS)*. IEEE, 2017, pp. 4110–4117.

[27] Z. He, F. Meng, X. Chen, Z. Yu, X. Fan, R. Sato, A. Ming, and Q. Huang, "Controllable height hopping of a parallel legged robot," *Applied Sciences*, vol. 11, no. 4, p. 1421, 2021.

[28] M. Bolignari, A. Mo, M. Fontana, and A. Badri-Spröwitz, "Diaphragm ankle actuation for efficient series elastic legged robot hopping," in *2022 IEEE/RSJ International Conference on Intelligent Robots and Systems (IROS)*. IEEE, 2022, pp. 4279–4286.

[29] A. De and D. E. Koditschek, "The penn jerboa: A platform for exploring parallel composition of templates," *arXiv preprint arXiv:1502.05347*, 2015.

[30] G. Wenger, A. De, and D. E. Koditschek, "Frontal plane stabilization and hopping with a 2dof tail," in *2016 IEEE/RSJ International Conference on Intelligent Robots and Systems (IROS)*. IEEE, 2016, pp. 567–573.

[31] D. W. Haldane, M. M. Plecnik, J. K. Yim, and R. S. Fearing, "Robotic vertical jumping agility via series-elastic power modulation," *Science Robotics*, vol. 1, no. 1, p. eaag2048, 2016.

[32] D. W. Haldane, J. K. Yim, and R. S. Fearing, "Repetitive extreme-acceleration (14-g) spatial jumping with salto-1p," in *2017 IEEE/RSJ International Conference on Intelligent Robots and Systems (IROS)*. IEEE, 2017, pp. 3345–3351.

[33] C. Kim, D.-J. Lee, S.-P. Jung, and G.-P. Jung, "Dipo: a miniaturized hopping robot via lightweight and compact actuator design for power amplification," *Bioinspiration & Biomimetics*, vol. 18, no. 4, p. 046006, 2023.

[34] C. A. Aubin, R. H. Heisser, O. Peretz, J. Timko, J. Lo, E. F. Helbling, S. Sobhani, A. D. Gat, and R. F. Shepherd, "Powerful, soft combustion actuators for insect-scale robots," *Science*, vol. 381, no. 6663, pp. 1212–1217, 2023.

[35] Y. Chen, H. Wang, E. F. Helbling, N. T. Jafferis, R. Zufferey, A. Ong, K. Ma, N. Gravish, P. Chirarattananon, M. Kovac *et al.*, "A biologically inspired, flapping-wing, hybrid aerial-aquatic microrobot," *Science robotics*, vol. 2, no. 11, p. eaao5619, 2017.

[36] P. Aerts, "Vertical jumping in galago senegalensis: the quest for an obligate mechanical power amplifier," *Philosophical Transactions of the Royal Society of London. Series B: Biological Sciences*, vol. 353, no. 1375, pp. 1607–1620, 1998.

[37] W. D. Shin, H.-V. Phan, M. A. Daley, A. J. Ijspeert, and D. Floreano, "Fast ground-to-air transition with avian-inspired multifunctional legs," *Nature*, vol. 636, no. 8041, pp. 86–91, 2024.

[38] Z. He, F. Meng, X. Fan, R. Kang, S. Liu, H. Liu, Z. Yu, M. Qin, A. Ming, and Q. Huang, "Development of a parallel-elastic robot leg for loaded jumping," in *2019 IEEE 4th International Conference on Advanced Robotics and Mechatronics (ICARM)*. IEEE, 2019, pp. 420–425.

[39] V. Klemm, A. Morra, C. Salzmann, F. Tschopp, K. Bodie, L. Gulich, N. Küng, D. Mannhart, C. Pfister, M. Vierneisel *et al.*, "Ascento: A two-wheeled jumping robot," in *2019 International Conference on Robotics and Automation (ICRA)*. IEEE, 2019, pp. 7515–7521.

[40] J. K. Yim, E. K. Wang, and R. S. Fearing, "Drift-free roll and pitch estimation for high-acceleration hopping," in *2019 International Conference on Robotics and Automation (ICRA)*. IEEE, 2019, pp. 8986–8992.

[41] J. K. Yim, B. R. P. Singh, E. K. Wang, R. Featherstone, and R. S. Fearing, "Precision robotic leaping and landing using stance-phase balance," *IEEE Robotics and Automation Letters*, vol. 5, no. 2, pp. 3422–3429, 2020.

[42] M. H. Raibert, *Legged robots that balance*. MIT press, 1986.

[43] Y.-H. Hsiao, S. Bai, Z. Guan, S. Kim, Z. Ren, P. Chirarattananon, and Y. Chen, "Hybrid locomotion at the insect scale: Combined flying and jumping for enhanced efficiency and versatility," *Science Advances*, vol. 11, no. 15, p. eadu4474, 2025.

[44] S. Li, S. Bai, R. Jia, Y. Cai, R. Ding, Y. Shi, F. Zhang, and P. Chirarattananon, "A high-payload robotic hopper powered by bidirectional thrusters," *IEEE Transactions on Robotics*, 2025.

[45] P. Foehn, A. Romero, and D. Scaramuzza, "Time-optimal planning for quadrotor waypoint flight," *Science robotics*, vol. 6, no. 56, p. eabh1221, 2021.

[46] A. Romero, S. Sun, P. Foehn, and D. Scaramuzza, "Model predictive contouring control for time-optimal quadrotor flight," *IEEE Transactions on Robotics*, vol. 38, no. 6, pp. 3340–3356, 2022.

[47] S. Sun, A. Romero, P. Foehn, E. Kaufmann, and D. Scaramuzza, "A comparative study of nonlinear mpc and differential-flatness-based control for quadrotor agile flight," *IEEE Transactions on Robotics*, vol. 38, no. 6, pp. 3357–3373, 2022.

[48] B. Brown and G. Zeglin, "The bow leg hopping robot," in *Proceedings. 1998 IEEE International Conference on Robotics and Automation (Cat. No. 98CH36146)*, vol. 1. IEEE, 1998, pp. 781–786.

[49] C. Liu and M. Plecnik, "Experimental validation of the usage of kinematic singularities to produce periodic high-powered motion," in *2022 International Conference on Robotics and Automation (ICRA)*. IEEE, 2022, pp. 11 402–11 408.

[50] J. G. Nichol, S. P. Singh, K. J. Waldron, L. R. Palmer Iii, and D. E. Orin, "System design of a quadrupedal galloping machine," *The International Journal of Robotics Research*, vol. 23, no. 10-11, pp. 1013–1027, 2004.

[51] U. Scarfogliero, C. Stefanini, and P. Dario, "A bioinspired concept for high efficiency locomotion in micro robots: the jumping robot grillo," in *Proceedings 2006 IEEE International Conference on Robotics and Automation, 2006. ICRA 2006.* IEEE, 2006, pp. 4037–4042.

[52] A. Degani, S. Feng, H. B. Brown, K. M. Lynch, H. Choset, and M. T. Mason, "The parkourbot-a dynamic bowleg climbing robot," in *2011 IEEE International Conference on Robotics and Automation*. IEEE, 2011, pp. 795–801.

[53] B. Zhu, J. Xu, A. Charway, and D. Saldaña, "Pogodrone: Design, model, and control of a jumping quadrotor," in *2022 International Conference on Robotics and Automation (ICRA)*. IEEE, 2022, pp. 2031–2037.

[54] S. Burns and M. Woodward, "Design and control of a high-performance hopping robot," *IEEE Robotics and Automation Letters*, 2025.

[55] N. C. Sharp, "Animal athletes: a performance review," *Veterinary Record*, vol. 171, no. 4, pp. 87–94, 2012.

[56] W. M. Poplin and C. A. Poplin, "Acceleration modeling with constant power," SAE Technical Paper, Tech. Rep., 2023.

[57] G. Kenneally, A. De, and D. E. Koditschek, "Design principles for a family of direct-drive legged robots," *IEEE Robotics and Automation Letters*, vol. 1, no. 2, pp. 900–907, 2016.

[58] B. Katz, J. Di Carlo, and S. Kim, "Mini cheetah: A platform for pushing the limits of dynamic quadruped control," in *2019 International Conference on Robotics and Automation (ICRA)*. IEEE, 2019, pp. 6295–6301.

[59] A. L. Brill, A. De, A. M. Johnson, and D. E. Koditschek, "Tail-assisted rigid and compliant legged leaping," in *2015 IEEE/RSJ International Conference on Intelligent Robots and Systems (IROS)*. IEEE, 2015, pp. 6304–6311.

[60] T. J. Roberts and E. Azizi, "Flexible mechanisms: the diverse roles of biological springs in vertebrate movement," *Journal of experimental biology*, vol. 214, no. 3, pp. 353–361, 2011.

[61] D. Morgan, U. Proske, and D. Warren, "Measurements of muscle stiffness and the mechanism of elastic storage of energy in hopping kangaroos." *The Journal of physiology*, vol. 282, no. 1, pp. 253–261, 1978.

[62] B. A. Christensen, D. C. Lin, M. J. Schwaner, and C. P. McGowan, "Elastic energy storage across speeds during steady-state hopping of desert kangaroo rats (dipodomys deserti)," *Journal of Experimental Biology*, vol. 225, no. 2, p. jeb242954, 2022.

[63] S. Van Wassenbergh, J. A. Strother, B. E. Flammang, L. A. Ferry-Graham, and P. Aerts, "Extremely fast prey capture in pipefish is powered by elastic recoil," *Journal of the Royal Society interface*, vol. 5, no. 20, pp. 285–296, 2008.

[64] W. D. Shin, W. Stewart, M. A. Estrada, A. J. Ijspeert, and D. Floreano, "Elastic-actuation mechanism for repetitive hopping based on power modulation and cyclic trajectory generation," *IEEE Transactions on Robotics*, vol. 39, no. 1, pp. 558–571, 2022.

[65] S. N. Patek, B. Nowroozi, J. Baio, R. L. Caldwell, and A. P. Summers, "Linkage mechanics and power amplification of the mantis shrimp's strike," *Journal of Experimental Biology*, vol. 210, no. 20, pp. 3677–3688, 2007.

[66] F. Ito, Y. Ishii, S. Kurumaya, K. Kagaya, and T. Nakamura, "A design method for instantaneous force generation based on a mantis shrimp with exoskeleton spring," *IEEE/ASME Transactions on Mechatronics*, vol. 29, no. 2, pp. 960–971, 2024.

[67] D. A. Pabst, "Springs in swimming animals," *American Zoologist*, vol. 36, no. 6, pp. 723–735, 1996.

[68] S. Longo, S. Cox, E. Azizi, M. Ilton, J. Olberding, R. St Pierre, and S. Patek, "Beyond power amplification: latch-mediated spring actuation is an emerging framework for the study of diverse elastic systems," *Journal of Experimental Biology*, vol. 222, no. 15, p. jeb197889, 2019.

[69] S. Bai, R. Ding, and P. Chirarattananon, "A micro aircraft with passive variable-sweep wings," *IEEE Robotics and Automation Letters*, vol. 7, no. 2, pp. 4016–4023, 2022.

[70] S. Bai, Q. He, and P. Chirarattananon, "A bioinspired revolving-wing drone with passive attitude stability and efficient hovering flight," *Science Robotics*, vol. 7, no. 66, p. eabg5913, 2022.

[71] G. A. Pratt, "Legged robots at mit: what's new since raibert?" *IEEE Robotics & Automation Magazine*, vol. 7, no. 3, pp. 15–19, 2000.

[72] X. Yun, E. R. Bachmann, and R. B. McGhee, "A simplified quaternion-based algorithm for orientation estimation from earth gravity and mag-

netic field measurements," *IEEE Transactions on instrumentation and measurement*, vol. 57, no. 3, pp. 638–650, 2008.

[73] C. Rucker, "Integrating rotations using nonunit quaternions," *IEEE Robotics and Automation Letters*, vol. 3, no. 4, pp. 2979–2986, 2018.

[74] L. Wang, Z. Zhang, and P. Sun, "Quaternion-based kalman filter for ahrs using an adaptive-step gradient descent algorithm," *International Journal of Advanced Robotic Systems*, vol. 12, no. 9, p. 131, 2015.

[75] Z. Batts, J. Kim, and K. Yamane, "Untethered one-legged hopping in 3d using linear elastic actuator in parallel (leap)," in *International Symposium on Experimental Robotics*. Springer, 2016, pp. 103–112.

[76] A. Muhr, "Modeling the stress-strain behavior of rubber," *Rubber chemistry and technology*, vol. 78, no. 3, pp. 391–425, 2005.

[77] G. Spedding and P. Lissaman, "Technical aspects of microscale flight systems," *Journal of Avian Biology*, pp. 458–468, 1998.

[78] Y. Lee, K.-B. Lua, T. Lim, and K. Yeo, "A quasi-steady aerodynamic model for flapping flight with improved adaptability," *Bioinspiration & biomimetics*, vol. 11, no. 3, p. 036005, 2016.

[79] J. Shi *et al.*, "Good features to track," in *1994 Proceedings of IEEE Conference on Computer Vision and Pattern Recognition*. IEEE, 1994, pp. 593–600.

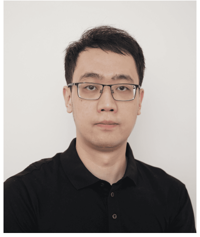

Songnan Bai received a B.S. degree in mechanical engineering from Xi'an Jiaotong University, Xi'an, China, in 2017, an M.Sc. in Mechanical Engineering from City University of Hong Kong, Hong Kong SAR, and a Ph.D. degree in Biomedical Engineering from City University of Hong Kong, Hong Kong SAR.

He is currently a research assistant professor in the Department of Civil Engineering, University of Hong Kong, Hong Kong SAR. His research interests include micro air vehicles, legged robots and multimodal robots.

Runze Ding received his B.S. degree in Aircraft Power Engineering in 2015 and his M.Phil. degree in Aerospace Propulsion Theory in 2019, both from Nanjing University of Aeronautics and Astronautics, Nanjing, China, and a Ph.D. degree from City University of Hong Kong, Hong Kong SAR.

He is currently a Professor with the School of Automation, Southeast University, Nanjing, China. His research interests include the design and control of robotic systems, with a focus on micro aerial robots and hybrid-locomotion robots.

Song Li received the B.E. degree in Flight Vehicle Design from Xi'an Jiaotong University, Shaanxi, China, in 2020, and the M.E. degree in Flight Vehicle Design from Beihang University, Beijing, China, in 2023.

He is currently a visiting research student at the University of Toronto, Canada, and pursuing a Ph.D. degree in Biomedical Engineering at City University of Hong Kong, Hong Kong SAR, China. His research interests include bio-inspired robotics, hopping robots, micro air vehicles, and flapping-wing robots.

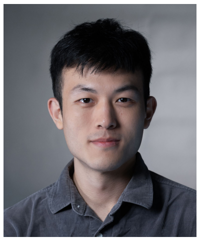

Ruihan Jia received the B.E. degree in mechatronic engineering from the University of Sydney, Sydney, NSW, Australia, in 2023.

He is currently working toward the M.Phil. degree in Biomedical Engineering with the Department of Biomedical Engineering, City University of Hong Kong, Hong Kong SAR, China. His research interests include micro aerial vehicles, dynamics, and robotic perception.

Ruobing Wang received the B.Eng. and M.Eng. degrees in Mechanical Engineering from Nanjing University of Aeronautics and Astronautics, Nanjing, China, in 2017 and 2020, respectively, and the Ph.D. degree in Industrial Engineering from The Hong Kong Polytechnic University, Hong Kong, in 2023.

He is currently a Postdoctoral Fellow with the Department of Biomedical Engineering, City University of Hong Kong, Hong Kong. His research interests include aerial robotics, parallel manipulators, and cable-driven mechanisms.

Zhiyuan Zhang received the B.E. degree in computer science in 2021 and the M.Eng. degree in computer science in 2023, both from Harbin Institute of Technology (Shenzhen), Shenzhen, China.

He is currently pursuing a joint Ph.D. degree with the Department of Biomedical Engineering, City University of Hong Kong, Hong Kong SAR, China, and the Department of Computer Science, Harbin Institute of Technology (Shenzhen), Shenzhen, China. His research interests include bio-inspired robots, reinforcement learning, and flapping-wing robots.

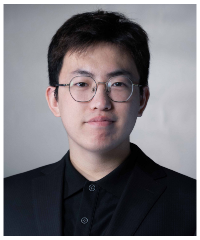

Fangzheng Wang received the B.E. degree in vehicle engineering from Southwest University, Chongqing, China, in 2021, and the M.S. degree in human and biological robotics from Imperial College London, London, U.K., in 2022.

He is currently pursuing the M.Phil. degree in biomedical engineering with the City University of Hong Kong, , Hong Kong SAR, China.

Pakpong Chirarattananon (S'12-M'15) received a B.A. degree in Natural Sciences from the University of Cambridge, U.K., and a Ph.D. degree in Engineering Sciences from Harvard University, Cambridge, MA, USA.

He is currently an Associate Professor at the Department of Mechanical & Industrial Engineering, University of Toronto, Toronto, Canada. Prior to this, he was a faculty member at City University of Hong Kong, Kowloon, Hong Kong SAR, China. His research interests include bio-inspired robots, micro air vehicles, and the applications of control and dynamics in robotic systems.